The Journal of Chemical Physics

Modeling cross-flow ultrafiltration of permeable particle dispersions

Cite as: J. Chem. Phys. **153**, 204110 (2020); https://doi.org/10.1063/5.0020986
Submitted: 06 July 2020 . Accepted: 06 November 2020 . Published Online: 30 November 2020

Gun Woo Park, and Gerhard Nägele

The Journal of Chemical Physics ARTICLE scitation.org/journal/jcp

Modeling cross-flow ultrafiltration of permeable particle dispersions

Cite as: J. Chem. Phys. 153, 204110 (2020); doi: 10.1063/5.0020986
Submitted: 6 July 2020 • Accepted: 6 November 2020 •
Published Online: 30 November 2020

Gun Woo Park[a] and Gerhard Nägele[b]

AFFILIATIONS

Institute of Biological Information Processing, IBI-4, Forschungszentrum Jülich GmbH, 52425 Jülich, Germany

[a]Author to whom correspondence should be addressed: g.park@fz-juelich.de
[b]Electronic mail: g.naegele@fz-juelich.de

ABSTRACT

Cross-flow ultrafiltration is a pressure-driven separation and enrichment process of small colloidal particles where a colloidal feed dispersion is continuously pumped through a membrane pipe permeable to the solvent only. We present a semi-analytic modified boundary layer approximation (mBLA) method for calculating the inhomogeneous concentration-polarization (CP) layer of particles near the membrane and the dispersion flow in a cross-flow filtration setup with a hollow fiber membrane. Conditions are established for which unwarranted axial flow and permeate flow reversal are excluded, and non-monotonic CP profiles are observed. The permeate flux is linked to the particle concentration on the membrane wall using the Darcy–Starling expression invoking axially varying osmotic and trans-membrane pressures. Results are discussed for dispersions of hard spheres serving as a reference system and for solvent-permeable particles mimicking non-ionic microgels. Accurate analytic expressions are employed for the concentration and solvent permeability dependent dispersion viscosity and gradient diffusion coefficient entering into the effective Stokes flow and advection–diffusion equations. We show that the mBLA concentration and flow profiles are in quantitative agreement with results by a finite element method. The mBLA results are compared with predictions by an earlier CP layer similarity solution, showing the higher precision of the former method.

I. INTRODUCTION

Membrane ultrafiltration (UF) is a pressure-driven process for the concentration and purification of dispersions of (colloidal) particles undergoing strong Brownian motion, having the major advantage of low energy consumption. It is extensively used for water purification, protein enrichment, blood treatment by (artificial) kidneys, and the reuse of oil droplets.[1–3]

Different from nanofiltration where the mean pore size of the membrane is an order-of-magnitude smaller than that in UF, the retained larger particles in UF are dispersed but not dissolved in the low-molecular-weight solvent. In both UF and nanofiltration, Brownian motion and the associated trans-membrane osmotic pressure are important effects. UF needs to be distinguished further from the so-called microfiltration of larger, micrometer-sized particles where Brownian motion and osmotic pressure effects are negligible, but out-of-equilibrium hydrodynamic effects such as shear-induced diffusion come into play.[2,4,5]

A standard way of operating UF is the inside-out cross-flow mode, where a feed dispersion is pumped steadily through a bundle of (typically cylindrical) hollow fiber membranes with inlet and outlet ports (cf. Fig. 1). The particle-enriched dispersion is collected at the outlet port. Ideally, the fiber membrane is only solvent-permeable. Its material properties (e.g., mean pore size, thickness, and stiffness) and its geometrical properties (e.g., inner radius R and length L of the cylinder) are selected depending on the solute, solvent, and operating conditions. Owing to the applied trans-membrane pressure (TMP), a small fraction of the in-flowing solvent permeates the membrane from the lumen side to the outside of the fiber into the permeate bath. Given an ideally particle-retentive membrane, the particles are thereby retained inside the

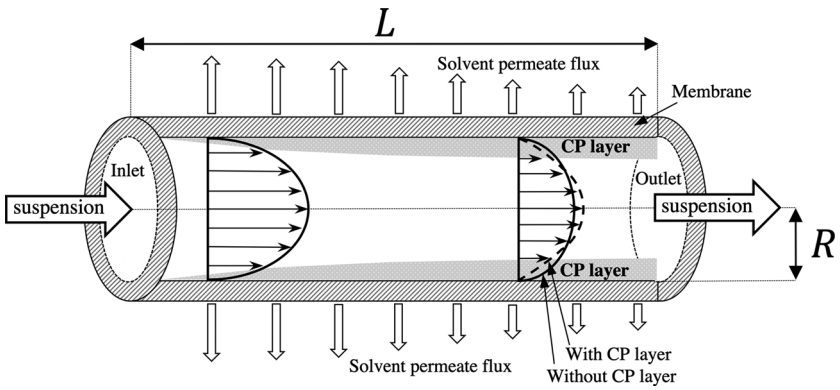

FIG. 1. Schematics of cross-flow, inside-out filtration in a cylindrical membrane pipe of length L and inner radius R. The thickness of the CP layer (in gray) is exaggerated for improved visibility and likewise the distortion (dashed curve) of the pure-solvent parabolic axial velocity profile caused by the CP layer.

fiber. Consequently, a non-homogeneous particle-enriched diffuse layer is formed near the inner membrane wall, which, in general, becomes more pronounced with increasing axial distance from the fiber inlet. This so-called concentration-polarization (CP) layer is determined by the balance of gradient diffusion away and flow convection toward the wall. The increased viscosity in the CP layer slows down the dispersion flow, which further enhances polarization. A consequential osmotic pressure buildup in the CP layer counteracts the TMP, causing a reduced inside-out permeate flux of the solvent associated with a lowered filtration efficiency. It is, therefore, important to minimize concentration polarization in order to maintain a significant permeate flux. In a filtration experiment, the CP layer contributes to a less than a linear increase in the mean permeate flux with increasing values of the mean TMP.

To quantify CP layer effects in cross-flow UF, it is useful as a reference to analyze first the cross-flow of pure solvent in a porous tube without dispersed particles. In UF systems, the radial fluid velocity inside the lumen region is commonly small compared to the axial velocity, while the axial variations of velocity fields are small compared to the radial ones. One can simultaneously consider the combined pure-solvent flow inside the lumen, membrane, and permeate (extracapillary) parts of the UF setup, as done in calculations in Refs. 5–7 for stationary, laminar, and incompressible flow conditions, by combining the Stokes and Darcy equations outside and inside the membrane, respectively. The flows are coupled at the cylindrical membrane–fluid interfaces on assuming the zero tangential velocity boundary condition, which is reasonable since the hydraulic membrane resistance is high. This gives rise to a pressure inside the lumen and a TMP across the membrane, which both decrease with a hyperbolic functional dependence for increasing axial distance from the inlet.[6]

Instead of considering explicitly the intra-membrane and permeate flow parts, it is expedient to simply couple the searched-for interior lumen flow to the outside using an appropriate membrane law at the inner membrane surface. Original work along these lines was done by Berman,[8] who calculated the flow profile in a rectangular pipe, followed by the work of Yuan and Finkelstein[9] for a cylindrical pipe. They assumed a pressure-independent constant radial suction velocity at the inner membrane surface, giving rise to a lumen pressure profile decreasing quadratically in the axial direction. This physically unreasonable membrane law was later replaced by the Darcy–Starling equation, linearly relating the local radial suction (permeate) velocity to the local TMP, in accord with the observation that the pressure gradient inside the membrane is dominated by the TMP.[10] Using the Darcy–Starling equation, a hyperbolic form of the axial pressure drop inside the lumen is recovered.[10–13]

When a dispersion is filtrated under UF conditions, the development of the CP layer at the inner membrane surface changes the permeate flux and the (dispersion) flow profile in comparison to those of the pure solvent. The mean thickness of the CP layer is, in general, small compared with the inner radius R of the membrane fiber. Therefore, a boundary layer analysis is commonly used in CP layer modeling. A boundary layer analysis for a steady-state CP layer invokes a one-dimensional balance of the radial convection current toward and the radial gradient (collective) diffusion current of particles away from the inner membrane wall.[14] The axial convection of particles is hereby accounted for only indirectly via a mass transfer coefficient.[14,15] In quantifying the overall intensity of the CP layer, the excess particle flux is commonly determined in this matched asymptotic analysis[4,6,16] by invoking the global conservation of particles inside the lumen for a fully particle-retentive membrane.

A few remarks are in order here regarding earlier theoretical works on CP layers, described based on a boundary layer analysis. Within a one-dimensional radial boundary layer analysis, axial convection can be accounted for globally using the constancy of the cross-sectionally integrated particle flux[17–19] for known flow and concentration profiles in the lumen. This constancy is due to the conservation of particles inside the lumen for a fully particle retentive membrane. Denisov,[19] in particular, has presented a detailed matched asymptotic expansion in inverse powers of a radial Péclet number by using, for simplicity, constant values for the gradient diffusion coefficient and dispersion viscosity, in conjunction with the linear van't Hoff expression for the osmotic pressure, which is valid for low particle concentrations only. Similarly, the model proposed by Elimelech and co-workers[17,18] also invokes global particle conservation and the constancy of the

gradient diffusion coefficient and viscosity. In addition, a parabolic profile is assumed in their model for the longitudinal dispersion velocity.

In a different steady-state boundary layer analysis where the advection–diffusion balance equation in the CP layer includes both axial and radial particle convection, a similarity solution for the CP concentration profile was obtained.[16,20–23] On the basis of this similarity solution, the CP layer and permeate flux profiles in cross-flow UF were calculated in two studies by Roa *et al.*[23,24] for dispersions of charge-stabilized particles and for a model of solvent-permeable particles mimicking non-ionic microgels, respectively. In these studies, accurate analytic expressions were used for the concentration-dependent gradient diffusion coefficient, dispersion viscosity, and osmotic pressure.

In this work, we present a modified boundary layer analysis method, referred to as the mBLA method, and an associated finite element method (FEM) of calculating the CP layer and flow profiles for cross-flow UF of dispersions of non-permeable and solvent permeable particles inside a hollow fiber membrane. The mBLA and FEM calculations are based on the effective Stokes equation for dispersion flow, the advection–diffusion equation, and the Darcy–Starling equation accounting for the dispersion osmotic pressure, with the concentration and solvent-permeability dependencies of the involved transport coefficients included. Using a leading-order regular perturbation expansion, we discuss first analytic expressions for the pressure and velocity profiles in the pure solvent case. This allows for determining the range of UF operating conditions for which unwarranted effects such as axial flow exhaustion (AFE) and permeate flow reversal (PFR) are avoided. In PFR, the trans-membrane flow changes along the filter pipe from suction to injection caused by a strong axial pressure drop.

The pure-solvent result is used as the input to the outer dispersion flow solution in our ensuing leading-order matched asymptotic expansion boundary layer analysis of the CP layer in UF. To elucidate the effects of the concentration and permeability dependence of the transport coefficients on UF, we consider first a reference system with constant values of the dispersion viscosity and collective diffusion coefficient, which allows for essentially analytic treatment. While the same radial variation of the flow profile is obtained as in the pure solvent case, the axial flow variation is different for a dispersion, owing to the coupling of the flow to the CP concentration profile determining the osmotic pressure contribution in the Darcy–Starling equation. In a dominant balance analysis of axial–radial convection and radial diffusion contributions to the CP layer, three different cases must be distinguished depending on the operation conditions. For the practically relevant operating conditions considered in this work, the case of a one-dimensional radial advection–diffusion balance is obtained in the boundary layer with the according inner solution for concentration-dependent dispersion properties. The inner solution is asymptotically matched to the outer solution in an open functional form. By enforcing the conservation of particles inside the lumen volume, the CP profile is finally determined using a fixed-point iteration (FPI) scheme.

The only input parameters characterizing the dispersion are the concentration-dependent gradient diffusion coefficient D, dispersion viscosity η, and osmotic pressure Π. Explicit results are discussed for model dispersions of impermeable and solvent-permeable hard spheres (HS), for which in both cases, accurate analytic expressions for the input quantities are provided.[25] The excellent accuracy of our mBLA results for the CP layer concentration field and permeate flow is demonstrated by the comparison with numerical results obtained by elaborate FEM calculations. We further show that the mBLA results are in distinctly better agreement with the FEM data than a similarity solution prediction for the CP layer employed in an earlier work.[23]

Fouling is not considered in the present work, which focuses on *generic* CP layer effects in UF on both concentration and flow fields and which involves a precise modeling of relevant transport properties. Fouling is an undesirable modification (e.g., hydraulic resistance enlargement) of the membrane caused by *specific* physico–chemical interactions between the membrane and particles, causing stagnant particle cake layer formation, adsorption of particles at the membrane wall, and clogging of membrane pores by intruding particles. The operating conditions in this work are such that reversible cake layer formation by particles becoming immobilized due to crystallization or jamming is avoided.

This paper is organized as follows: In Sec. II, we describe the macroscopic cross-flow UF model with its underlying transport equations and boundary and operating conditions. The essentials of our finite element (FEM) numerical scheme are given in Appendix A. Analytic expressions for the transport properties of solvent-permeable particles with hard-core interactions used as the input to the mBLA and FEM calculations are discussed in Sec. III, in conjunction with the associated Appendix B. Section IV includes our perturbation analysis of the UF model. After introducing the relevant base units and dimensionless quantities, in Sec. IV A, we first describe the analytic regular perturbation expansion solution for pure solvent flow. This is followed in Sec. IV B by explaining our mBLA method for the concentration and flow profiles for dispersions with concentration-dependent transport properties. We account here for the axially varying osmotic pressure at the inner membrane wall. The results, given in Sec. V, consist of three subsections. In Sec. V A, we discuss velocity and pressure profiles for pure solvent flow, and we analyze criteria for axial flow exhaustion and permeate flow reversal. For a reference system of colloidal hard spheres, in Sec. V B, we compare the semi-analytic mBLA results with the according FEM data showing quantitative agreement. Furthermore, we compare with the concentration profile results by a previous similarity solution for the CP layer.[23] The effect of the solvent permeability of particles on cross-flow UF is analyzed in Sec. V C. Our conclusions are presented in Sec. VI. Salient details of the mBLA method are summarized in Appendixes C and D.

II. CROSS-FLOW ULTRAFILTRATION MODEL

Consider with Fig. 1 a monodisperse feed dispersion of neutrally buoyant, rigid, and spherical Brownian particles of hard-core radius a steadily pumped through a hollow cylindrical fiber membrane of inner radius $R \gg a$, length L, and radius-to-length aspect ratio,

$$\epsilon = R/L \ll 1. \tag{1}$$

On a coarse-grained length scale where the size a of dispersed particles and the morphology of the membrane channels are not resolved, the mass and momentum transport in the dispersion undergoing UF are governed by macroscopic continuum mechanics equations. Mass balance, i.e., particle number conservation, is described by the continuity equation $\partial\phi/\partial t + \nabla\cdot\mathbf{J} = 0$, where $\phi(\mathbf{r},t) = (4\pi a^3/3)n(\mathbf{r},t)$ is the (dispersion-averaged) local volume fraction of particles at position $\mathbf{r}$ and time t. Moreover, $n(\mathbf{r}, t)$ is the associated local number density, and $\mathbf{J}(\mathbf{r}, t)$ the local particle flux. Under UF conditions, the flow is laminar and the dispersion of Brownian particles is only slightly driven out of equilibrium. Hence, $\mathbf{J} = \mathbf{J}_d + \mathbf{J}_{ad}$ is the sum of a diffusion flux, $\mathbf{J}_d = -D(\phi)\nabla\phi$, related to thermal Brownian motion, whose strength at a local volume fraction ϕ is quantified by the equilibrium gradient or (long-time) collective diffusion coefficient $D(\phi)$, and an advection flux, $\mathbf{J}_{ad} = \phi\mathbf{V}$, where $\mathbf{V}(\mathbf{r}, t)$ is the local dispersion velocity. Substitution of the above expression for $\mathbf{J}$ into the continuity equation leads to the advection–diffusion equation,

$$\frac{\partial\phi}{\partial t} + \mathbf{V}\cdot\nabla\phi = \nabla\cdot(D(\phi)\nabla\phi), \tag{2}$$

where, in addition, the incompressibility constraint,

$$\nabla\cdot\mathbf{V} = 0, \tag{3}$$

for macroscopic dispersion flow was used.

Under low-Reynolds-number conditions met in UF, the momentum balance for the dispersion-averaged, incompressible laminar flow is described by the effective Stokes equation,

$$\nabla P = \eta(\phi)\Delta\mathbf{V} + \frac{d\eta}{d\phi}\nabla\phi\cdot\left[\nabla\mathbf{V} + (\nabla\mathbf{V})^T\right], \tag{4}$$

invoking, in addition to $\mathbf{V}$, the dispersion-averaged local pressure P and the low-shear dispersion viscosity $\eta(\phi)$. Moreover, UF is performed under low-shear conditions where non-Newtonian effects are negligible. Hence, $P(\mathbf{r}) = p_f(\mathbf{r}) + \Pi(\phi(\mathbf{r}))$ is the sum of the equilibrium osmotic pressure, Π, due to the Brownian particles phase and a fluid-phase pressure contribution, p_f, adjusting itself such that the incompressibility constraint in Eq. (3) is maintained.[26] The effective Stokes equation includes a force density proportional to $d\eta/d\phi$, which is non-zero in the inhomogeneous CP layer region. Since in a colloidal dispersion solvent, vorticity diffusion is much faster than particle diffusion, the steady-state dispersion flow described by the linear Stokes equation is established much faster than the steady-state CP layer profile $\phi(\mathbf{r})$. While we are concerned, in this paper, with steady-state UF, in the FEM calculations, it is advantageous to start from the advection–diffusion equation including the explicit time derivative of ϕ (see below).

For cross-flow operating conditions compatible with the cylindrical geometry of the membrane fiber, there is axisymmetric dispersion flow without swirling, i.e.,

$$\mathbf{V}(\mathbf{r}) = v(r,z)\hat{\mathbf{r}} + u(r,z)\hat{\mathbf{z}}, \tag{5}$$

with cylindrical coordinates (r, z) and radial and axial unit vectors $\hat{\mathbf{r}}$ and $\hat{\mathbf{z}}$, respectively. Here, $v(r, z)$ and $u(r, z)$ are the radial and axial velocity components, respectively. We use the operating (boundary) conditions

$$\begin{aligned}\phi(r, z=0) &= \phi_b,\\ P(r, z=0) &= P_{in},\\ P(r, z=L) &= P_{out},\\ P(R+h, z) &= P_{perm},\end{aligned} \tag{6}$$

where ϕ_b is the small volume fraction of the uniform feed dispersion at the inlet cross section $z = 0$ and h is the constant thickness of the membrane. The dispersion flow is driven by a constant pressure difference $P_{in} > P_{out}$, where P_{in} and P_{out} are the pressure values at the inlet and outlet cross sections of the fiber, respectively. Both pressure values are taken as larger than the constant pressure inside the permeate, P_{perm}, which typically equals the atmospheric pressure. Alternative to P_{in} and P_{out}, one can specify the longitudinal pressure difference, $\Delta_L P = P_{in} - P_{out}$, and the fiber-length averaged TMP,

$$\Delta_T P = \frac{1}{L}\int_0^L (P(R,z) - P_{perm})dz, \tag{7}$$

where $P(R, z)$ for $0 \le z \le L$ is the pressure profile at the inner membrane wall, which is *a priori* unknown. As an approximation for $\Delta_T P$, one can use instead the mean TMP,

$$\Delta_T^{(l)} P = \frac{1}{2}(P_{in} + P_{out}) - P_{perm}, \tag{8}$$

where the superscript (l) denotes the trans-membrane pressure of a linearly declining axial pressure profile inside the lumen, corresponding to a membrane with very low solvent permeability where the flow is of the Hagen–Poiseuille (HP) type. As discussed in Sec. IV A, the relative difference between $\Delta_T P$ and $\Delta_T^{(l)} P$ in the lumen is small in UF and the radial pressure variation is negligible in comparison to the axial one. Thus, in setting $P_{out} = 1$ atm, only the specification of $\Delta_L P$ and $\Delta_T^{(l)} P$ as the physical control parameters is required.

We assume the hollow fiber membrane to be fully retentive to the colloidal particles. This amounts to using the zero normal particle flux (i.e., reflective) boundary condition at the inner membrane wall, i.e.,

$$\phi_w(z)v_w(z) - D(\phi_w(z))\left.\frac{\partial\phi}{\partial r}\right|_{r=R} = 0. \tag{9}$$

Here, $v_w(z) = v(R, z)$ is the radial permeate velocity, which is of positive sign in the inside-out direction, and $\phi_w(z) = \phi(R, z)$ is the volume fraction of particles, with both quantities evaluated at the lumen-side membrane wall. On starting from a general irreversible thermodynamics description, the reflective boundary condition is recovered from the second integrated Kedem–Katchalsky equation of cross-membrane transport in the limit of negligible cross-membrane particle diffusion and advection (see Ref. 2).

The mean solvent velocity, $\mathbf{V}_s$, inside the fully wetted cylindrical membrane sheet ($R \le r \le R + h$) of thickness h can be described by the local Darcy equation $\mathbf{V}_s = -(\kappa/\eta_s)\nabla P$, where κ is the Darcy permeability of the uniform membrane and η_s is the solvent shear viscosity.[6,7] The characteristic axial velocity inside the membrane,

$u_m = \kappa\Delta_L P/(\eta_s L)$, is distinctly smaller than that inside the lumen, $u_{HP} = R^2\Delta_L P/(4\eta_s L)$, with the latter estimated by the Hagen–Poiseuille (HP) value for the longitudinal velocity along the membrane pipe axis, since $u_m/u_{HP} = 4\kappa/R^2 \ll 1$. This supports our usage of the zero slip tangential boundary condition,[10]

$$u(r = R, z) = 0, \tag{10}$$

at the inner membrane wall.

Different from the lumen region, the axial pressure variation inside the membrane, estimated as $|\partial P/\partial z| \sim \Delta_L P/L$, is much smaller than the radial trans-membrane pressure variation, $|\partial P/\partial r| \sim \Delta_T P/h$. This allows for a purely radial integration of the local Darcy equation across the thickness of the membrane, giving rise to a logarithmic pressure profile and a mean solvent velocity profile equal to[27]

$$v_s(r) = \frac{\kappa(P(R) - P_{perm})}{\eta_s \ln\left(1 + \frac{h}{R}\right)}\frac{1}{r}, \tag{11}$$

where $R \le r \le R + h$. Using $v_w = v_s(R)$ and replacing $P(R)$ by $P(R) - \Pi(\phi_w)$ to account for the osmotic pressure results in the Darcy–Starling law,

$$v_w(z) = L_P[\,P(R, z) - P_{perm} - \Pi(\phi_w(z))\,], \tag{12}$$

where

$$L_P = \frac{\kappa}{\eta_s R \ln\left(1 + \frac{h}{R}\right)} \tag{13}$$

is the hydraulic solvent permeability of the membrane. The parameter L_P is determined by an UF experiment using a clean membrane and pure solvent. Typical values of L_P for UF are in the range of 10^{-11} – 10^{-10} m/(Pa s).[2] The Darcy–Starling law in Eq. (12) includes the local osmotic pressure profile $\Pi(\phi_w(z))$ at the inner membrane wall counteracting the local TMP, $P(R, z) - P_{perm}$, at axial distance z from the inlet. Starting likewise from irreversible thermodynamics, the Darcy–Starling law is recovered from the first integrated Kedem–Katchalsky equation in the limit of an ideally particle-reflective membrane and a pure-solvent permeate.[2] Notice that the Stokes equation of lumen flow in Eq. (4) is coupled to the advection–diffusion equation via the Darcy–Starling law and the concentration dependence of the dispersion viscosity.

The task is to obtain a (numerical) solution of the governing equations for the cylindrical cross-flow UF model described in this section. For a full numerical solution, we have used a finite-element method (FEM) integrated into the COMSOL Multiphysics software (version 5.3). This COMSOL software was used already in earlier studies of cross-flow filtration processes (see Refs. 28 and 29). Salient details of our implementation of the FEM method are given in Appendix A.

The major contribution of this paper is the development and application of a semi-analytic so-called modified boundary layer approximation (mBLA) method for the concentration and flow profiles of the present UF model. As we are going to show, the results by the mBLA method are in excellent agreement with the elaborated FEM results. Remarkably, our C++ implementation of the mBLA method is typically a thousand times faster than the corresponding FEM calculations. Even our mBLA Python code is about 10–20 times faster than the FEM calculations. The Python code for calculating UF properties using the mBLA method is freely available.[30]

III. PROPERTIES OF SOLVENT-PERMEABLE PARTICLES

The only input to the UF model in Sec. II consists of the dispersion transport properties D and η and the dispersion equilibrium osmotic pressure Π. In UF, the Brownian particles are subject to flow conditions where the single-particle shear-Péclet number fulfills $Pe_a = \dot{\gamma}a_h^2/D_0 \ll 1$. Here, $\dot{\gamma}$ is a characteristic shear rate of UF cross-flow, and

$$D_0 = \frac{k_B T}{6\pi\eta_s a_h} \tag{14}$$

is the Stokes–Einstein–Sutherland single-particle diffusion coefficient, with the hydrodynamic particle radius a_h, Boltzmann's constant k_B, and dispersion temperature T. Using a Hagen–Poiseuille flow profile, the low-Pe_a condition transforms into

$$1\,\text{nm}^3 \lesssim a_h^3 \ll \frac{k_B T}{3\pi\epsilon\Delta_L P}. \tag{15}$$

The left inequality is due to the condition that the considered particles are dispersed and not dissolved. For example, using $\Delta_L P = 130$ Pa and $\epsilon = 10^{-3}$, with water at room temperature as the solvent, Eq. (15) implies that 1 nm $\lesssim a_h <$ 150 nm. At low-Pe_a, the microstructure of dispersions is only slightly perturbed away from its isotropic equilibrium form without flow.

We use here a generic so-called hydrodynamic radius model (HRM) for dispersions of monodisperse, solvent-permeable spherical particles with internal hydrodynamic structure and (effective) hard-core direct interactions. Dispersions in case whose dynamic properties are well described by this model are non-ionic and strongly cross-linked microgel dispersions[23,25] and core–shell spherical colloids.[31] The permeable particles behave hydrodynamically like no-slip spheres, immersed in a structureless Newtonian fluid under low-Reynolds-number flow conditions. They are globally characterized by a hydrodynamic radius a_h somewhat smaller than the hard-core radius a. The hydrodynamic radius a_h can be related to particle-specific properties and, here, particularly to the (mean) Darcy permeability κ_p whose square-root, $\sqrt{\kappa_p}$, is the hydrodynamic penetration depth. For uniformly permeable particles of constant reduced inverse penetration depth $\zeta = a/\sqrt{\kappa_p}$, the relation between the reduced hydrodynamic radius γ and ζ is[32]

$$\gamma \equiv \frac{a_h(\zeta)}{a} = \frac{2\zeta^2(\zeta - \tanh(\zeta))}{2\zeta^3 + 3(\zeta - \tanh(\zeta))} = 1 - \frac{1}{\zeta} + \mathcal{O}\left(\frac{1}{\zeta^2}\right). \tag{16}$$

This relation expresses that a_h decreases monotonically with increasing permeability. We have introduced here the Landau big-$\mathcal{O}$ symbol for which $A = \mathcal{O}(B)$ means here that $A/B \to \text{const} \neq 0$ for $B \to 0$.

Despite its simplicity, the HRM is universally applicable since hydrodynamic corrections to model-based dynamic transport properties such as D and η are quite small, i.e., of quadratic order in the

reduced slip length $\bar{\gamma} = 1 - \gamma$ and in $1/\zeta$.[32] Therefore, hard spherical particles with differing (radially varying) internal hydrodynamic structure are all well described by the HRM, provided $\gamma > 0.8$, which encompasses many experimentally studied dispersions.

The general expression for the dispersion viscosity η at low-Pe_a is

$$\eta(\phi;\gamma) = \eta_\infty(\phi;\gamma) + \Delta\eta(\phi;\gamma), \tag{17}$$

where η_∞ is the high-frequency limiting shear viscosity and $\Delta\eta(\phi;\gamma)$ is the shear relaxation viscosity part related to non-instantaneous configurational shear-stress relaxations.

The gradient (i.e., long-time collective) diffusion coefficient $D(\phi;\gamma)$ in the advection–diffusion equation in Eq. (2) is only slightly smaller than the associated short-time collective diffusion coefficient, even at high volume fractions close to the freezing transition value. Therefore, we can approximate $D(\phi;\gamma)$ to good accuracy by the short-time coefficient[25]

$$D(\phi;\gamma) \approx D_0(\gamma)\frac{K(\phi;\gamma)}{S(\phi)}, \tag{18}$$

appearing on the right-hand side of this equation. Here, $K(\phi;\gamma)$ is the short-time sedimentation coefficient, and $S(\phi)$ is the osmotic compressibility factor. Moreover, $D_0(\gamma) = k_BT/(6\pi\eta_s\gamma a)$. For the HRM of permeable hard spheres, convenient analytic expressions are available for the gradient diffusion coefficient $D(\phi;\gamma)$ and low-shear viscosity $\eta(\phi;\gamma)$.[23,25] These expressions are summarized in Appendix B. For $\gamma > 0.8$ and hard-core volume fractions ϕ up to the freezing transition value $\phi_f = 0.494$, they give results in good agreement with high-precision simulation data.[32]

The concentration dependencies of the viscosity and gradient diffusion coefficient are obtained from the expressions in Appendix B and are depicted in Figs. 2(a) and 2(b), respectively. Values for the reduced hydrodynamic radius considered in this study are $\gamma = \{1, 0.979, 0.888, 0.763\}$, corresponding to an inverse reduced solvent penetration depth $\zeta = \{\infty, 50, 10, 5\}$, respectively. As noticed from the figure, the influence of permeability on the transport properties is significant at high volume fractions. Notice further that different from the self-diffusion coefficient, the gradient diffusion coefficient increases with increasing concentration. While the viscosity decreases with increasing permeability (i.e., decreasing γ), the opposite trend is observed for gradient diffusion. As shown in Sec. V C, the influence of the solvent permeability of particles on the wall concentration profile $\phi_w(z)$ becomes significant for non-small distances z from the inlet, even though the inlet concentration ϕ_b is taken to be very small (i.e., $\phi_b = 10^{-3}$).

In addition to D and η, the CP layer is influenced by the osmotic pressure Π at the membrane wall. For the hard particles of the HRM model, we use the Carnahan–Starling equation of state,

$$\Pi(\phi) = \frac{k_BT}{V_a}\phi\frac{\left(1+\phi+\phi^2-\phi^3\right)}{(1-\phi)^3}, \tag{19}$$

where $V_a = (4/3)\pi a^3$ is the particle volume and a is the hard-core radius. This expression is valid to high accuracy up to the freezing transition. Note that $\Pi \propto 1/a^3$, i.e., the osmotic pressure decreases strongly with increasing particle radius. For charged particles not considered here, there is an additional contribution to the osmotic pressure arising from (screened) electrostatic interactions.[24,33]

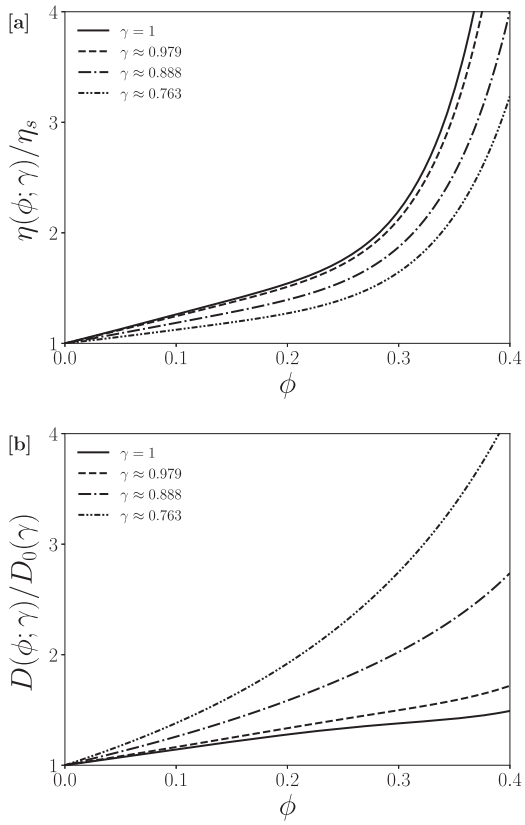

FIG. 2. (a) Dispersion viscosity, $\eta(\phi;\gamma)$, in units of the solvent viscosity η_s and (b) gradient diffusion coefficient, $D(\phi;\gamma)$, divided by the single-particle diffusion coefficient $D_0(\gamma)$ of a dispersion of permeable spheres as functions of particle volume fraction ϕ. Values of the reduced hydrodynamic radius γ are as indicated.

IV. PERTURBATION ANALYSES

In this section, we derive semi-analytic expressions for the UF flow and concentration fields in the lumen region. This is achieved using regular and singular perturbation analyses performed to leading order in the small quantities $\epsilon = R/L \ll 1$ and $\epsilon_\delta = \delta_{CP}/R \ll 1$, respectively, where δ_{CP} characterizes summarily the thickness of the CP boundary layer. As will be shown in this section using a dominant balance analysis of the advection–diffusion equation, δ_{CP} is determined as $D_0/(L_P\Delta_T^{(l)}P)$.

We discuss first the regular perturbation analysis of pure-solvent flow. This is followed by a singular perturbation (matched asymptotic) analysis of the CP layer profile for dispersion flow, resulting in our semi-analytic mBLA method where the volume concentration field ϕ of the CP layer is determined using a numerical procedure. While our analysis of pure-solvent flow resembles that in the recent work by Tilton *et al.*,[10] we use different base units appropriate for the extension to the dispersion case where ϕ_b is non-zero. Our discussion of the pure-solvent case is not only a necessary prerequisite for the mBLA method describing dispersion UF but also further provides analytic criteria for identifying unwarranted axial

flow exhaustion (AFE) and permeate flow reversal (PFR) operating conditions.

Before going into the perturbation analyses of pure-solvent and dispersion flows, we first introduce the relevant dimensionless quantities and according base units and explain the employed general notation. For any physical quantity f, its dimensionless form is labeled by a tilde,

$$\tilde{f} = \frac{f}{f^*}, \tag{20}$$

where f^* is a base (characteristic) unit of f. Base units are labeled here by an asterisk. For convenience, the base units for the flow properties u, v, and P and the radial and axial distances r and z, respectively, are formed using directly accessible input parameters. Explicitly, we employ the base units

$$\begin{gathered} r^* = R, \quad z^* = L, \\ u^* = u_{HP}, \quad v^* = L_P \Delta_T^{(l)} P, \quad P^* = \Delta_L P. \end{gathered} \tag{21}$$

Here, u^* is the axial flow velocity along the pipe axis, identified with the Hagen–Poiseuille parabolic laminar flow field u_{HP}. For the latter to apply, the confining pipe material has to be impermeable, corresponding to $\kappa = 0$. Moreover, v^* is the radial permeate velocity in the pure solvent case (where $\Pi = 0$), with the mean TMP in Eq. (12) approximated by $\Delta_T^{(l)} P$. The selected base unit for pressure quantities is $\Delta_L P$, which renders $\partial \tilde{P}/\partial \tilde{z} \sim \mathcal{O}(1)$ into a derivative of order one.

The Reynolds number for cylindrical pipe flow is $Re = u^* R/\nu_s$, where $\nu_s = \eta_s/\rho_s$ is the kinematic viscosity and ρ_s is the mass density of the solvent, the former equal to $\nu_s \approx 10^{-6}$ m^2/s for water at room temperature. Laminar flow requires that $Re \lesssim 2000$, and the absence of inertial flow effects implies[10]

$$\epsilon Re \ll 1. \tag{22}$$

As two suitable dimensionless operating parameters, we introduce first α given by the ratio of mean TMP and $\Delta_L P$,

$$\alpha = \frac{\Delta_T P}{\Delta_L P} \quad \text{and} \quad \alpha^* = \frac{\Delta_T^{(l)} P}{\Delta_L P}, \tag{23}$$

and second the solvent recovery indicator β defined by

$$\beta = \frac{Q_{perm}}{Q_{in}} \quad \text{and} \quad \beta^* = \frac{4 v^*}{\epsilon u^*}. \tag{24}$$

Here,

$$\begin{aligned} Q_{in} &= 2\pi \int_0^R u(r, z=0)\, r\, dr, \\ Q_{perm} &= 2\pi R \int_0^L v_w(z)\, dz \end{aligned} \tag{25}$$

are the dispersion volume flow rate through the pipe inlet, Q_{in}, and the permeate volume flow rate, Q_{perm}, through the hollow fiber membrane, respectively. The associated base units α^* and β^* are taken as the analytic values of α and β for pure Hagen–Poiseuille longitudinal flow u_{HP} and pure-solvent transversal permeate flow v_w without osmotic pressure contribution in the Darcy–Starling equation. The ratio of the two base units,

$$k^2 = \frac{\beta^*}{\alpha^*} = \frac{16}{\epsilon^2} \frac{\eta_s L_P}{R}, \tag{26}$$

defines another dimensionless parameter k of interest, characterizing the overall solvent permeability of the membrane and the longitudinal pressure drop across the pipe length. The typical range of $\eta_s L_p/R$ for an UF membrane is $10^{-10} - 10^{-14}$.[10] For $\epsilon = 10^{-3}$, the parameter k is thus quite small, attaining values in the range of $10^{-1} - 10^{-4}$.

Note that the pressure ratio α^* in combination with $k = \sqrt{\beta^*/\alpha^*}$, or alternatively the characteristic value β^* for the solvent recovery indicator in combination with k, fully characterizes the dimensionless operating conditions for pure solvent flow (cf. Sec. IV A). In the case of dispersion flow discussed in Sec. IV B, one needs to specify additionally a radial Péclet Pe_R introduced in Eq. (37), as well as the inlet concentration ϕ_b, which we select equal to 10^{-3} for all considered dispersions. As shown in Secs. IV A and IV B, it holds that

$$\begin{aligned} \tilde{P}_{in} - \tilde{P}_{perm} &= \alpha^* + \frac{1}{2} = \frac{\beta^*}{k^2} + \frac{1}{2}, \\ \tilde{P}_{out} - \tilde{P}_{perm} &= \alpha^* - \frac{1}{2} = \frac{\beta^*}{k^2} - \frac{1}{2}. \end{aligned} \tag{27}$$

Hence, the pressure operating conditions can be expressed in terms of α^* alone. The above noted dimensionless operating parameters are profitably used to characterize the systems discussed in Sec. V.

A. Pure solvent flow: Regular perturbation

For pure solvent flow in the lumen volume ($0 < r < R$ and $0 < z < L$) without dispersed particles, there is no steady-state boundary layer. We can thus apply a zeroth-order regular perturbation expansion in the small fiber aspect ratio ϵ, leading to an analytic solvent flow solution. From this solution, operating criteria are obtained, which allow identifying unwarranted AFE and PFR effects. These criteria are used in our study of the cross-flow UF of dispersions.

The incompressibility constraint and the radial and longitudinal components of the Stokes equation describing laminar non-inertial flow are given in non-dimensional form by

$$\begin{aligned} 0 &= \frac{\beta^*}{4}\left[\frac{\partial \tilde{v}}{\partial \tilde{r}} + \frac{\tilde{v}}{\tilde{r}}\right] + \frac{\partial \tilde{u}}{\partial \tilde{z}}, \\ \frac{\partial \tilde{P}}{\partial \tilde{r}} &= \epsilon^2 \beta^* \left(\frac{\partial^2 \tilde{v}}{\partial \tilde{r}^2} + \frac{1}{\tilde{r}}\frac{\partial \tilde{v}}{\partial \tilde{r}} - \frac{\tilde{v}}{\tilde{r}^2} + \epsilon^2 \frac{\partial^2 \tilde{v}}{\partial \tilde{z}^2}\right), \\ 4\frac{\partial \tilde{P}}{\partial \tilde{z}} &= \frac{\partial^2 \tilde{u}}{\partial \tilde{r}^2} + \frac{1}{\tilde{r}}\frac{\partial \tilde{u}}{\partial \tilde{r}} + \epsilon^2 \frac{\partial^2 \tilde{u}}{\partial \tilde{z}^2}, \end{aligned} \tag{28}$$

respectively. Moreover, the non-dimensional form of the Darcy–Starling equation for pure solvent flow is

$$\tilde{v}_w(\tilde{z}) = \frac{1}{\alpha^*}\left(\tilde{P}(\tilde{z}) - \tilde{P}_{perm}\right), \tag{29}$$

with $\tilde{P}(\tilde{z}=0)=\tilde{P}_{in}$ and $\tilde{P}(\tilde{z}=1)=\tilde{P}_{out}$ denoting the dimensionless pressures at the inlet and outlet, respectively.

Before applying regular perturbation, the order of magnitude of the base unit β^* needs to be assessed in relation to ϵ. In the case of a small $\beta^* = \mathcal{O}(\epsilon)$, the purely longitudinal Hagen–Poiseuille flow inside a solvent-impermeable pipe is recovered from Eq. (28) in the zeroth-order regular perturbation limit $\epsilon \to 0$. Thus, $\beta^* \gg \epsilon$ is required for the flow field to be affected by the non-zero solvent permeability of the membrane. In the opposite case of large $\beta^* = \mathcal{O}(1/\epsilon)$, the longitudinal velocity $\tilde{u}$ in Eq. (28) is neglected to zeroth order in ϵ and a radial flow solution is obtained, which is incompatible with the axial symmetry requirement $v(r=0,z)=0$.

Therefore, we assume that $\epsilon \ll \beta^* \ll 1/\epsilon$, with according constraints for the base unit α^* in Eq. (26), for a given value of k. While the incompressibility constraint [i.e., the first equation in Eq. (28)] and thus fluid volume conservation remain unaffected to the zeroth order in ϵ, terms of $\mathcal{O}(\epsilon^2)$ are discarded in the radial and longitudinal parts of the Stokes equation. The radial part implies thus a radially constant pressure field $\tilde{P} = \tilde{P}(\tilde{z})$. The other two partial differential equations are solved by separation of variables using $\tilde{u}(\tilde{r},\tilde{z}) = \tilde{u}_R(\tilde{r})\tilde{u}_Z(\tilde{z})$ and $\tilde{v}(\tilde{r},\tilde{z}) = \tilde{v}_R(\tilde{r})\tilde{v}_w(\tilde{z})$. The radial velocity variations are determined as $\tilde{u}_R(\tilde{r}) = 1-\tilde{r}^2$ and $\tilde{v}_R(\tilde{r}) = 2\tilde{r}-\tilde{r}^3$. Note that $\tilde{u}_R$ is of the Hagen–Poiseuille form, while $\tilde{v}_R$ agrees with the according leading-order radial velocity dependence reported in Ref. 9. The axial variation of the velocity and pressure fields is determined by the coupled ordinary differential equations,

$$\frac{d\tilde{P}}{d\tilde{z}} = -\tilde{u}_Z(\tilde{z}) \quad \text{and} \quad \frac{d\tilde{u}_Z}{d\tilde{z}} = -\beta^*\tilde{v}_w(\tilde{z}). \tag{30}$$

In conjunction with the zero tangential slip, axisymmetry, and Darcy–Starling boundary conditions, $u(r=R,z)=0$, $v(r=0,z)=0$, and $v(r=R,z)=v_w(z)$ with $v_w(z)$ in Eq. (12), respectively, Eq. (30) leads to the analytic flow solution,

$$\begin{aligned}
\tilde{P}(\tilde{z}) - \tilde{P}_{perm} &= A_+ e^{k\tilde{z}} + A_- e^{-k\tilde{z}},\\
\tilde{u}(\tilde{r},\tilde{z}) &= -k(1-\tilde{r}^2)\left(A_+ e^{k\tilde{z}} - A_- e^{-k\tilde{z}}\right),\\
\tilde{v}(\tilde{r},\tilde{z}) &= \frac{1}{\alpha^*}(2\tilde{r}-\tilde{r}^3)\left(\tilde{P}(\tilde{z}) - \tilde{P}_{perm}\right),
\end{aligned} \tag{31}$$

with coefficients

$$A_\pm = \pm\frac{1}{4\sinh(k)}\left[2\alpha^* - 1 - (2\alpha^*+1)e^{\mp k}\right]. \tag{32}$$

The above flow solution is valid to the zeroth order in ϵ.

Since the pressure condition relations in Eq. (27) follow directly from Eq. (31), this reproduces the $\mathcal{O}(\epsilon^0)$ flow solution in Refs. 10 and 13 by noting that in these earlier works, Q_{in} was specified instead of the inlet pressure P_{in}. According to Eqs. (30) and (31), the hyperbolic (exponential) pressure drop from $\tilde{P}_{in}$ at $\tilde{z}=0$ to $\tilde{P}_{out}$ at $\tilde{z}=1$ is of convex form provided $d^2\tilde{P}/d\tilde{z}^2 = \beta^*\tilde{v}_w(\tilde{z}) > 0$. The faster linear pressure decay is due to fluid sucked out through the permeable ($k>0$) membrane into the permeate. In the limit $k\to 0$, i.e., for $\beta \to 0$, the linear pressure decay, $\tilde{P} = \tilde{P}_{in} - \tilde{z}$, of Hagen–Poiseuille flow inside a non-permeable tube is recovered, together with $\tilde{v}=0$ and $\tilde{u} = 1-\tilde{r}^2$.

Given that $P_{in} > P_{out}$ (i.e., $\Delta_L P > 0$), unwarranted permeate flow reversal (PFR) at the inner membrane wall from suction ($\tilde{v}_w > 0$) to injection ($\tilde{v}_w < 0$) takes place. PFR happens when the local TMP, $\tilde{P}(\tilde{z}) - \tilde{P}_{perm}$, changes its sign from positive to negative at an axial distance $\tilde{z} = \tilde{z}_{PFR} < 1$. Solvent injection across the membrane from the permeate reservoir into the lumen taking place for $\tilde{z} > \tilde{z}_{PFR}$ gives rise, according to Eq. (30), to a minimal $\tilde{u}_Z(\tilde{z})$ and hence a minimal cross-sectional volume flow rate $Q(z)$ at $\tilde{z} = \tilde{z}_{PFR}$. The criterion for no PFR along the full fiber length is thus $\tilde{P}_{out} > \tilde{P}_{perm}$ or equivalently $\alpha^* > 1/2$. Stated alternatively, for PFR to occur, it must hold that $\tilde{P}_{in} > \tilde{P}_{perm} > \tilde{P}_{out}$.

Another unwarranted effect is axial flow exhaustion (AFE), triggered by a mean TMP, which is large in comparison to $\Delta_L P$ (i.e., for large α^*), where the axial velocity $\tilde{u}(\tilde{r},\tilde{z})$ is reversed for axial distances $\tilde{z}$ from the inlet exceeding $\tilde{z}_{AFE} < 1$. In effect, fluid is sucked now into the fiber interior both from the inlet and outlet reservoirs. According to Eq. (30), $\tilde{P}(\tilde{z})$ and hence $\tilde{v}_w(\tilde{z})$ are minimal at this $\tilde{z}_{AFE}$. The condition for the absence of AFE along the membrane fiber is thus $\tilde{P}'(\tilde{z}=1) < 0$, where the prime denotes derivative with respect to $\tilde{z}$. Owing to fluid volume conservation, this condition is equivalent to $Q_{perm} < Q_{in}$ or likewise to $\beta < 1$.

In summary, PFR and AFE are both absent provided that

$$\frac{1}{2} < \alpha^* < \alpha^*_{max}(k) = \frac{1}{2}\cdot\frac{\cosh(k)+1}{\cosh(k)-1} = \frac{2}{k^2} + \frac{1}{3} + \mathcal{O}(k^2) \tag{33}$$

for given parameter k. The second inequality is the condition for no AFE, and the $\mathcal{O}(k^2)$ expansion of $\alpha^*_{max}(k)$ is sufficiently accurate for $k \lesssim 0.1$.

As a numerical illustration, Fig. 3(a) depicts the non-dimensional axial velocity $\tilde{u} = u/u_{HP}$ and the normalized TMP $(P_{out}-P_{perm})/\Delta_T^{(l)}P = 1 - 1/(2\alpha^*)$, both taken at the outlet position $\tilde{z}=1$, for a given $k \approx 0.1464$ as used in Ref. 23, corresponding to $\alpha^*_{max}(k) = 93.6$. Thus, no PFR and AFE are observed for operating conditions such that $0.5 < \alpha^* < 93.6$, implying that $0.01 < \beta^* = \alpha^* k^2 < 2.01$. Note that $\beta^* = 2.01$ corresponds to $\beta = 1$. For $\alpha^* \le 1/2$, the permeate flux near the outlet is reversed, as schematically depicted in Fig. 3(b), while for $\alpha^* \ge 93.6$, the axial flow is exhausted and then reversed near the outlet, as illustrated in Fig. 3(c). Since $\alpha^* \to 0$ implies $\beta^* \to 0$ for finite k, it follows that $\tilde{v}^* \to 0$. Consequently, Hagen–Poiseuille flow $\tilde{u}(0,\tilde{z}=1) = 1$ is recovered in this limit.

We conclude the discussion of pure solvent cross-flow by arguing that for conditions where PFR and AFE are avoided, the operating parameters α and β are of the same order of magnitude as the respective base units α^* and β^*, justifying hereby our usage of the latter ones. In the following, we show that $\alpha/\alpha^* = \Delta_T P/\Delta_T^{(l)}P$ and β/β^* are both of order one.

From the expression for the reduced pressure $\tilde{P}$ in Eq. (31), the ratios $\tilde{\alpha} = \alpha/\alpha^*$ and $\tilde{\beta} = \beta/\beta^*$ are obtained as

$$\begin{aligned}
\tilde{\alpha}(k) &= \frac{\Delta_T P}{\Delta_T^{(l)}P} = \frac{2}{k}\tanh\left(\frac{k}{2}\right) = 1 - \frac{k^2}{12} + \mathcal{O}(k^4),\\
\tilde{\beta}(k,\alpha^*) &= \frac{\tilde{\alpha}(k)}{\tilde{u}(0,0)} = \frac{4}{k^2}\frac{\cosh(k)-1}{1-2\alpha^*+(1+2\alpha^*)\cosh(k)},
\end{aligned} \tag{34}$$

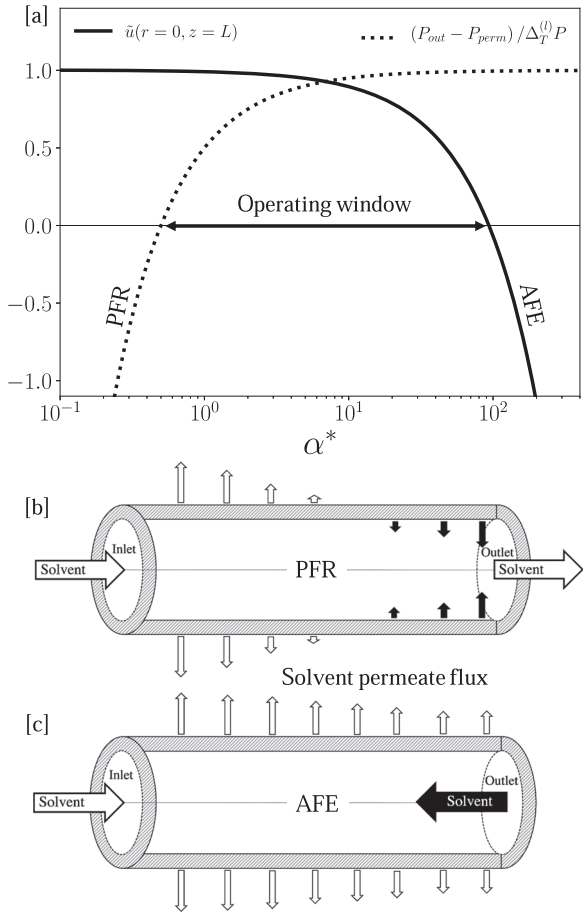

FIG. 3. (a) Normalized axial velocity $\tilde{u}(\tilde{r}=0,\tilde{z}=1)$ at the pipe axis and outlet (solid curve) and normalized trans-membrane pressure at the outlet (dotted curve) as functions of α^*. (b) Schematics of permeate flow reversal (PFR) where $\alpha^* < 1/2$ and (c) axial flow exhaustion (AFE) where $\alpha^* > \alpha^*_{max}(k) = 93.6$ for $k \approx 0.1464$.

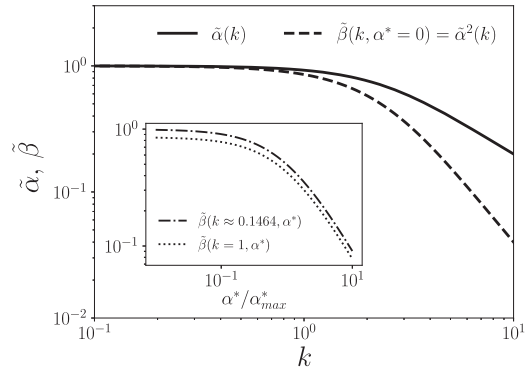

FIG. 4. Parameter ratios $\tilde{\alpha}=\alpha/\alpha^*$ and $\tilde{\beta}=\beta/\beta^*$, the latter at $\alpha^*=0$, as functions of k for pure solvent cross-flow. The inset shows $\tilde{\beta}(k,\alpha^*)$ in dependence of α^* divided by $\alpha^*_{max}(k)$ for $k \approx 0.1464$ and 1, respectively.

where $\tilde{u}(0,0) = \big(1-2\alpha^*+(1+2\alpha^*)\cosh(k)\big)k/(2\sinh(k))$ is the reduced axial velocity at the inlet center.

We first emphasize that α^* is independent of the membrane permeability and determined solely by the selected pressure conditions at the inlet, outlet, and permeate, while k is independent of the pressure operating conditions. Hence, α^* and k are a useful set of independent variables, the first one summarily characterizing the pressure operating conditions and the second one characterizing the membrane and solvent conditions. A small-k expansion of $\tilde{\alpha}$, $\tilde{\beta}$, and $\tilde{u}(0,0)$ shows that these quantities converge to unity as $k \to 0$, consistent with the recovery of Hagen–Poiseuille flow for zero membrane permeability.

Different from $\tilde{\alpha}(k)$, which is a function of the independent variable k only, $\tilde{\beta}(k,\alpha^*)$ depends additionally on the independent variable α^*. For $\alpha^*=0$, it is obtained that $\tilde{\beta}(k,\alpha^*=0)=\tilde{\alpha}^2(k)$. In the main part of Fig. 4, it is demonstrated on a double-logarithmic scale that $\tilde{\alpha}$ and $\tilde{\beta}$ at $\alpha^*=0$ are practically equal to one for values $k \lesssim 0.3$ typically encountered in UF processes.

The inset illustrates the α^*-dependence of $\tilde{\beta}$ for $k \approx 0.1464$ and $k=1$, respectively, where α^* has been non-dimensionalized by division through the maximally allowed value $\alpha^*_{max}(k)$ without AFE. One clearly notices that $\tilde{\beta} = \mathcal{O}(1)$ for $\alpha^* \le \alpha^*_{max}(k)$ even for the unrealistically large value $k=1$. The above considerations underscore the validity of the regular perturbation flow solution in Eq. (31) in terms of the parameters k and α^* for the operation window of α^* values in Eq. (33), which is depicted by the double arrow in Fig. 3(a). Up to this point, we have only considered pure-solvent flow. In the general case of dispersion cross-flow, the now present CP layer lowers the permeate flux compared with the pure-solvent case. The pure-solvent case constitutes thus the maximal permeation limit of dispersion cross-flow so that the operation window in Eq. (33) applies also to dispersions.

B. Dispersion flow: Singular perturbation

Having analyzed pure solvent cross-flow, we explain next our leading-order matched asymptotic analysis of stationary dispersion cross-flow UF for feed volume fractions $0 < \phi_b \ll 1$ where a stationary CP boundary layer is formed. In the framework of the continuum mechanics description introduced in Sec. II, the characteristic thickness of the CP layer, δ_{CP}, is small compared with the inner fiber radius R. Therefore, another smallness parameter $\epsilon_\delta = \delta_{CP}/R \ll 1$ comes into play in addition to the fiber aspect ratio ϵ, whose functional form is discussed further in the following. We assume that $\epsilon = o(\epsilon_\delta)$, where $o(\cdots)$ is the Landau small-o symbol, since ϵ is typically small compared to ϵ_δ. Here, $\epsilon = o(\epsilon_\delta)$ means that $\epsilon/\epsilon_\delta \to 0$ for $\epsilon_\delta \to 0$.

The advection–diffusion, incompressibility, and effective Stokes equations in Eqs. (2)–(4), respectively, are, to the linear order in ϵ, only regularly perturbed, which allows us to simply use their $\mathcal{O}(\epsilon^0)$ expressions. The first equation in Eq. (28) describing fluid incompressibility preserves, to $\mathcal{O}(\epsilon^0)$, its pure-solvent form, however, with $\tilde{v}(\tilde{r},\tilde{z})$ and $\tilde{u}(\tilde{r},\tilde{z})$ interpreted now as non-dimensional radial and axial components, respectively, of the steady-state dispersion

velocity $\mathbf{V}(\mathbf{r})$. The radial part of the Stokes equation shows that to $\mathcal{O}(\epsilon^0)$, the dispersion pressure, $\tilde{P} = \tilde{P}(\tilde{z})$, is independent of the radial variable as in the pure solvent case. The axial part of the Stokes equation reduces in $\mathcal{O}(\epsilon^0)$ to

$$4\frac{d\tilde{P}}{d\tilde{z}} = \frac{\partial}{\partial\tilde{r}}\left(\tilde{\eta}(\phi(\tilde{r},\tilde{z}))\frac{\partial\tilde{u}(\tilde{r},\tilde{z})}{\partial\tilde{r}}\right) + \frac{\tilde{\eta}(\phi(\tilde{r},\tilde{z}))}{\tilde{r}}\frac{\partial\tilde{u}(\tilde{r},\tilde{z})}{\partial\tilde{r}}, \tag{35}$$

where the reduced dispersion viscosity, $\tilde{\eta}(\phi) = \eta(\phi)/\eta_s$, is equal to one in the pure solvent limit $\phi = 0$. The steady-state form of the advection–diffusion Eq. (2) reduces to the zeroth order in ϵ to

$$\tilde{v}\frac{\partial\phi}{\partial\tilde{r}} + \frac{4}{\beta^*}\tilde{u}\frac{\partial\phi}{\partial\tilde{z}} = \frac{1}{Pe_R}\left[\frac{\partial}{\partial\tilde{r}}\left(\tilde{D}(\phi)\frac{\partial\phi}{\partial\tilde{r}}\right) + \frac{\tilde{D}(\phi)}{\tilde{r}}\frac{\partial\phi}{\partial\tilde{r}}\right], \tag{36}$$

where $\tilde{D}(\phi) = D(\phi)/D_0$ is the dimensionless gradient diffusion coefficient of the dispersion of value one for $\phi = 0$. For predominantly repulsive particle interactions, it holds $\tilde{D}(\phi) > 1$ for $\phi > 0$. Equation (36) states that the axial particle transport is dominated by advection.

The right-hand side of this equation is divided by the radial Péclet number,

$$Pe_R = \frac{Rv^*}{D_0}, \tag{37}$$

equal to the ratio of the diffusion time, R^2/D_0, and radial convection time, R/v^*, across a distance equal to the fiber radius R. A significant CP boundary layer is formed for $Pe_R \gg 1$, where radial advection of particles toward the membrane is distinctly faster than diffusion away from it. This is reflected in the singular perturbation of Eq. (36) with an associated smallness parameter $1/Pe_R \ll 1$. According to the Stokes–Einstein–Sutherland relation for D_0 in Eq. (14), a hydrodynamic particle radius a_h in the range of nanometers to micrometers corresponds to values of D_0 in the range of $10^{-10} - 10^{-13}$ m^2/s for water as the solvent at room temperature. For the values of the fiber radius R, membrane solvent hydraulic permeability L_p, and TMP used in the result Sec. V, the Péclet number $Pe_R \sim 78$ is large compared to one. Of additional relevance is the axial Péclet number $Pe_L = R^2u^*/(D_0L) = Pe_R(4/\beta^*)$, defined as the ratio of diffusion and axial convection times across a fiber length distance.

To derive an inner solution of flow and concentration fields inside the thin CP boundary layer, it is advantageous to use, instead of $\tilde{r}$, the reduced radial distance

$$\tilde{y} = 1 - \tilde{r} \tag{38}$$

from the membrane surface with a consequential sign change $\tilde{v} \to -\tilde{v}$ in the radial flow velocity. Inside the CP layer, we introduce a stretched radial coordinate $\bar{y}$ of $\mathcal{O}(1)$ defined by

$$\tilde{y} = \frac{\bar{y}}{\epsilon_\delta}. \tag{39}$$

In addition to the radial coordinate, the axial velocity requires stretching according to $\bar{u} = \tilde{u}/\epsilon_\delta$, owing to the zero tangential slip boundary condition at the membrane surface. An overbar is used to label stretched variables of $\mathcal{O}(1)$ inside the CP layer. Note that the non-dimensional dispersion pressure $\tilde{P}$, radial velocity $\tilde{v}$, and reduced axial distance $\tilde{z}$ from the inlet are all of $\mathcal{O}(1)$.

On neglecting the radial curvature term in Eq. (36) by noting that $1/\tilde{r} = \mathcal{O}(\epsilon_\delta)$ and considering that $\epsilon Re \ll 0$ and $\epsilon_\delta = o(\epsilon)$, the incompressibility, Stokes, and diffusion advection equations inside the boundary layer are obtained to leading orders in ϵ_δ as

$$\begin{aligned}\frac{\partial\bar{v}}{\partial\bar{y}} &= -\epsilon_\delta^2\frac{4}{\beta^*}\frac{\partial\bar{u}}{\partial\tilde{z}},\\ 4\epsilon_\delta\frac{\partial\tilde{P}}{\partial\tilde{z}} &= \frac{\partial}{\partial\bar{y}}\left(\tilde{\eta}(\phi)\frac{\partial\bar{u}}{\partial\bar{y}}\right),\\ \bar{v}\frac{\partial\phi}{\partial\bar{y}} + \epsilon_\delta^2\frac{4}{\beta^*}\bar{u}\frac{\partial\phi}{\partial\tilde{z}} &= \frac{1}{\epsilon_\delta Pe_R}\frac{\partial}{\partial\bar{y}}\left(\tilde{D}(\phi)\frac{\partial\phi}{\partial\bar{y}}\right),\end{aligned} \tag{40}$$

respectively.

We determine ϵ_δ now from a dominant balance analysis[34] of the boundary layer (i.e., inner) advection–diffusion equation in Eq. (40), where the radial diffusion term on the right-hand side is balanced on the left-hand side either by the radial convection term (case A), the transversal convection term (case B), or the sum of both of them (case AB). Recall that except for ϵ_δ, Pe_R, and base unit β^* of the solvent recovery indicator, all other parameters in this equation are of zeroth order in ϵ_δ. The outcome of this analysis for the functional dependence of ϵ_δ on the radial and axial Péclet numbers is listed in Table I, together with the according advection–diffusion equations to the zeroth order in ϵ_δ. Which of the three cases should be employed depends on the operating conditions.

In this paper, case A is used, complying to conditions found in many UF studies[19,23] where the formation of the CP layer is driven by the solvent permeation of the membrane. This is reflected by the dominant balance of the radial diffusion term by the radial advection term $\tilde{v}\partial\phi/\partial\bar{y} = \mathcal{O}(1)$, and it implies that $\epsilon_\delta Pe_R = \mathcal{O}(1)$. This, in turn, allows for identifying $\epsilon_\delta = 1/Pe_R$ and hence

$$\delta_{CP} = \frac{D_0}{v^*} = \frac{D_0}{L_P\Delta_T^{(l)}P} \tag{41}$$

as the characteristic CP layer thickness, as stated already at the beginning of this section. Furthermore, it holds that $\beta^*/4 \gg 1/Pe_R^2$, expressing the condition of significant solvent permeation of the membrane. In case A, a one-dimensional purely radial advection–diffusion is obtained, as noted in the table.

Case B describes a situation not relevant to UF studies where the solvent permeability of the membrane is very low, i.e., $\beta^*/4 = v^*/(\epsilon u^*) \ll 1/Pe_R^2$, and where, as a consequence, diffusion is dominantly balanced by axial advection. Here, ϵ_δ is of $\mathcal{O}(1/Pe_L^{1/3})$ as noted in the table. Case AB applies when diffusion is balanced on a similar level by radial and axial convection, from which it follows for moderate membrane permeabilities where $\beta^*/4 \sim 1/Pe_R^2$ that ϵ_δ is of the order of $1/Pe_R \sim 1/Pe_L^{1/3}$. Case AB has a similarity solution for the CP layer profile, which was used in several previous boundary layer theory studies of UF[15,21–23] based on the concept of mass transfer coefficients.

TABLE I. Dominant balance analysis of the advection–diffusion equation inside the CP layer. Depending on the operating conditions, three cases A, B, and AB are distinguished, with respective identification of the reduced CP layer thickness ϵ_δ in terms of axial and longitudinal Péclet numbers Pe_R and $Pe_L = Pe_R\,(4/\beta^*)$, respectively. Rightmost column lists the respective advection–diffusion equation to the zeroth order in ϵ_δ. Case A is used in this work and compared with the similarity CP layer solution of case AB.

Case	Condition	Identified ϵ_δ	Advection–diffusion equation
A	$\beta^*/4 \gg 1/Pe_R^2$	$\epsilon_\delta \sim 1/Pe_R$	$\tilde{v}\frac{\partial\phi}{\partial\tilde{y}} = \frac{\partial}{\partial\tilde{y}}\left(\tilde{D}\frac{\partial\phi}{\partial\tilde{y}}\right)$
B	$\beta^*/4 \ll 1/Pe_R^2$	$\epsilon_\delta \sim 1/Pe_L^{1/3}$	$\tilde{u}\frac{\partial\phi}{\partial\tilde{z}} = \frac{\partial}{\partial\tilde{y}}\left(\tilde{D}\frac{\partial\phi}{\partial\tilde{y}}\right)$
AB	$\beta^*/4 \sim 1/Pe_R^2$	$\epsilon_\delta \sim 1/Pe_R \sim 1/Pe_L^{1/3}$	$\tilde{v}\frac{\partial\phi}{\partial\tilde{y}} + \frac{4}{Pe_R^2\beta^*}\tilde{u}\frac{\partial\phi}{\partial\tilde{z}} = \frac{\partial}{\partial\tilde{y}}\left(\tilde{D}\frac{\partial\phi}{\partial\tilde{y}}\right)$

For case A conditions valid in most UF studies (see Refs. 19 and 23) for which $\epsilon_\delta = 1/Pe_R$, the three equations in Eq. (40) can be used for $\epsilon_\delta \to 0$. The resulting partial differential equations are integrated with respect to $\tilde{y}$ by invoking the reflective flux and zero tangential slip boundary conditions given in Eqs. (9) and (10), respectively. This leads to the following implicit integral equations for the radial and axial dispersion velocities and for the particle volume fraction in the inner boundary layer:

$$\begin{aligned}\tilde{v}^{in}(\tilde{z},[\phi_w]) &= -\tilde{v}_w(\tilde{z},[\phi_w]),\\ \tilde{u}^{in}(\tilde{y},\tilde{z},[\phi_w]) &= 2c(\tilde{z})\int_0^{\tilde{y}}\frac{1}{\tilde{\eta}}d\tilde{y}',\\ \phi^{in}(\tilde{y},\tilde{z},[\phi_w]) &= \phi_w(\tilde{z})e^{-\tilde{s}(\tilde{y},\tilde{z},[\phi_w])},\end{aligned} \tag{42}$$

where $\phi_w(\tilde{z}) = \phi^{in}(\tilde{y}=0,\tilde{z})$ is the volume concentration of particles right at the membrane wall. Moreover,

$$\begin{aligned}\tilde{s}(\tilde{y},\tilde{z},[\phi_w]) &= \tilde{v}_w(\tilde{z},[\phi_w])\int_0^{\tilde{y}}\frac{1}{\tilde{D}(\phi(\tilde{y}',\tilde{z},[\phi_w]))}d\tilde{y}',\\ 2c(\tilde{z}) &= \tilde{\eta}(\phi_w(\tilde{z}))\left.\frac{\partial\tilde{u}^{in}}{\partial\tilde{y}}\right|_{\tilde{y}\to 0}.\end{aligned} \tag{43}$$

The reduced dispersion viscosity $\tilde{\eta}$ and gradient diffusion coefficient $\tilde{D}$ are functions of $\phi^{in}(\tilde{y},\tilde{z},[\phi_w])$. Accurate analytic expressions for these transport properties and for the osmotic pressure Π are presented in Sec. III. As indicated, the inner solutions have a functional dependence on ϕ_w, which is still unknown at this point.

The full concentration and flow solutions follow from the asymptotic matching of the inner concentration and velocity solutions with the corresponding outer solutions in the bulk region outside the thin CP layer, the latter likewise considered to the zeroth order in ϵ. To obtain the outer solutions from the axial Stokes equation in Eq. (35) and the advection–diffusion equation in Eq. (36), notice that to the zeroth order in ϵ, the radial and axial velocity components $\tilde{v}$ and $\tilde{u}$ are still factorized in their $\tilde{r}$ and $\tilde{z}$ dependence such as in the pure solvent case for unchanged radial dependence as in Eq. (31). Their axial dependence, however, is determined now by the axial pressure variations according to the ordinary differential equations in Eq. (30) in conjunction with the non-dimensionalized generalized Darcy–Starling permeate flux law,

$$\tilde{v}_w(\tilde{z}) = \frac{1}{\alpha^*}\left(\tilde{P}(\tilde{z}) - \tilde{P}_{perm} - \tilde{\Pi}(\phi_w(\tilde{z}))\right), \tag{44}$$

for an ideally particle-reflective membrane and pure-solvent permeate, stating that the local TMP needs to exceed the local osmotic pressure at the membrane wall for having reverse osmotic solvent flow into the permeate. On solving the resulting inhomogeneous ordinary linear differential equations by variation of parameters, the outer flow solution is obtained as

$$\begin{aligned}\tilde{P}^{out}(\tilde{z},[\phi_w]) - \tilde{P}_{perm} &= (B_+[\phi_w] + g_-(\tilde{z},[\phi_w]))e^{k\tilde{z}}\\ &\quad + (B_-[\phi_w] + g_+(\tilde{z},[\phi_w]))e^{-k\tilde{z}},\\ \tilde{u}^{out}(\tilde{y},\tilde{z},[\phi_w]) &= \tilde{y}(2-\tilde{y})\tilde{u}_Z^{out}(\tilde{z},[\phi_w]),\\ \tilde{v}^{out}(\tilde{y},\tilde{z},[\phi_w]) &= -(1+\tilde{y}-3\tilde{y}^2+\tilde{y}^3)\tilde{v}_w(\tilde{z}),\end{aligned} \tag{45}$$

where $\tilde{u}_Z^{out} = -d\tilde{P}^{out}/d\tilde{z}$ and

$$g_\pm(\tilde{z},[\phi_w]) = \pm\frac{k}{2}\int_0^{\tilde{z}} e^{\pm k\tilde{z}'}\tilde{\Pi}(\phi_w(\tilde{z}'))d\tilde{z}', \tag{46}$$

$$B_\pm[\phi_w] = A_\pm \mp \frac{1}{2\sinh(k)}\left(g_+(1,[\phi_w])e^{-k} + g_-(1,[\phi_w])e^{k}\right), \tag{47}$$

with coefficients $A_\pm$ given in Eq. (32). Due to rotational symmetry with respect to the cylinder axis, $\tilde{v}^{out} = 0$ for $\tilde{y} = 1$.

The outer solution of Eq. (36) for the bulk volume fraction is

$$\phi^{out}(\tilde{y},\tilde{z}) = \phi_b, \tag{48}$$

consistent with $\phi(r, z=0) = \phi_b$, and obtained under the proviso that the feed volume concentration $\phi_b \lesssim \mathcal{O}(\epsilon_\delta)$ is small.

Having determined the inner and outer solutions up to their functional dependence on ϕ_w, the outer limit of the inner solution is now asymptotically matched to the inner limit of the outer solution. This matching is required for ϕ and $\tilde{u}$ only. To the zeroth order in ϵ_δ, the radial velocity is not steeply changing across the CP layer, and $\tilde{P}$ has no radial dependence at all.

Using Eqs. (42) and (45) in conjunction with a multiplicative mixing rule for $\tilde{u}$, an additive mixing rule for ϕ, and by expressing

$\tilde{y}$ in terms of $\tilde{r} = 1-\tilde{y}$ with an according sign change in $\tilde{v}$, the matched solutions are obtained as

$$\begin{aligned}\phi &= (\phi_w - \phi_b)e^{-\bar{s}} + \phi_b(1 - \bar{s}e^{-\bar{s}}),\\ \tilde{u} &= \tilde{u}_Z^{out}(1+\tilde{r})\int_{\tilde{r}}^{1}\frac{1}{\tilde{\eta}}d\tilde{r}',\\ \tilde{v} &= \tilde{v}^{out},\\ \tilde{P} &= \tilde{P}^{out},\end{aligned} \tag{49}$$

where arguments have been omitted for compactness of the notation. Details on the invoked matching procedures are given in Appendix C. Note that the dimensionless pressure operating expressions in Eq. (27), which are valid also for dispersion flow, are obtained from the pressure relations in Eqs. (45) and (49).

The matched asymptotic solutions for the concentration and flow fields are still functionally dependent on the wall concentration profile $\phi_w(\tilde{z})$. To determine this profile, we invoke as a global condition the cross-sectional particle-flux conservation law,

$$\Phi(z,[\phi_w]) = 2\pi\int_0^R j(r,z,[\phi_w])\,r\,dr = \Phi(0,[\phi_w]), \tag{50}$$

where

$$j(r,z,[\phi_w]) = \hat{\mathbf{z}}\cdot\mathbf{J}(r,z,[\phi_w]) = \phi(r,z,[\phi_w])\,u(r,z,[\phi_w]) \tag{51}$$

is the axial particles flux. We have disregarded here a negligibly small flux contribution arising from axial diffusion. Equation (50) states that for an ideally particle-retentive membrane and without fouling, the radially integrated steady-state axial particle flux, Φ, is constant, independent of z, for all membrane fiber cross sections. Using particle-flux conservation in conjunction with a fixed-point iteration (FPI) method, $\phi_w(z)$ is numerically determined, and after its substitution, the concentration and flow fields are determined using Eq. (49). Details on the iteration method are given in Appendix D. One notices from Eq. (49) that the concentration profile $\phi(\tilde{r},\tilde{z})$ inside and outside the boundary layer is only implicitly dependent on $\tilde{r}$ and $\tilde{z}$ through the single variable $\bar{s}(\tilde{r},\tilde{z})$ except for the $\tilde{z}$-dependence of the wall concentration profile $\phi_w(\tilde{z})$. The latter is determined by the particle-flux conservation law in Eq. (50).

The matched asymptotic solution in Eq. (49), in combination with particle number conservation and the FPI solver, constitute our modified boundary layer analysis mBLA method, allowing for a fast and accurate calculation of UF concentration and flow profiles. Results by this method are presented in Sec. V for permeable particle dispersions. We point out that the mBLA result in Eqs. (49) and (50) for case A does not apply at distances $z \lesssim L_D$ close to the inlet, where $L_D = L\,\epsilon_\delta^2/(4\beta^*)$ is the so-called development length of the stationary CP layer discussed in Refs. 19 and 35. The development length arises since inside a characteristic distance $\sim L_D$ from the inlet, axial convection cannot be neglected even in case A [see the advection–diffusion equation in Eq. (40)].

In the dilute limit of concentration-independent transport properties and zero osmotic pressure (i.e., for $\eta \approx \eta_s$, $D \approx D_0$, and $\Pi = 0$), the flow field is fully decoupled from the concentration field. The function $\bar{s}$ in Eq. (43) is here simply equal to $\bar{s}(\tilde{y},\tilde{z}) = \tilde{v}_w(\tilde{z})\tilde{y}$ with linear $\tilde{y}$ dependence. Thus, for constant transport properties $\tilde{D} = 1$ and $\tilde{\eta} = 1$, the radial decay of the concentration profile with increasing $\tilde{y}$ is basically a single exponential one. Notice here that the contribution $-\phi_b\bar{s}e^{-\bar{s}}$ in Eq. (49) is typically negligible for the non-small axial distances $\tilde{z}$ away from the inlet region. Using Eq. (D3) in Appendix D, we obtain here the simplified mBLA result,

$$\begin{aligned}\frac{\phi_w^{CT}(\tilde{z})}{\phi_b} \approx 1 + \frac{1}{8}\left(\frac{\tilde{u}_Z(0)}{\tilde{u}_Z(\tilde{z})} - 1\right)\left(\frac{\tilde{v}_w(\tilde{z})}{\epsilon_\delta} + 3\right)\frac{\tilde{v}_w(\tilde{z})}{\epsilon_\delta}\\ + 2\frac{\tilde{u}_Z(0)}{\tilde{u}_Z(\tilde{z})}\left(1 - \frac{\tilde{v}_w(\tilde{z})}{\tilde{v}_w(0)}\right)^2,\end{aligned} \tag{52}$$

where $\tilde{u}_Z(\tilde{z})$ and $\tilde{v}_w(\tilde{z})$ are the pure-solvent expressions given in Sec. IV A. The superscript (CT) labels properties obtained for constant transport coefficients. The approximation in Eq. (52) for ϕ_w is used in Sec. V.

In concluding our presentation of the semi-analytic mBLA method, we point to its virtues in comparison with the FEM calculations. First, its numerical evaluation is substantially faster while providing results in good agreements with the FEM calculations. Second, it gives physical insight into the functional forms of the concentration and flow profiles and the specific occurrence of the system parameters. We have exemplified this for the general $\phi(\tilde{r},\tilde{z})$ in Eq. (49) and the special $\phi_w^{(CT)}(\tilde{z})$ in Eq. (52). A thorough discussion of the mBLA method for the concentration and flow profiles is given in Sec. V.

V. RESULTS AND DISCUSSION

We start by describing the employed UF operating conditions and the membrane and dispersion parameters. Consider a hollow fiber membrane of length $L = 0.5$ m and inner radius $R = 0.5$ mm (i.e., $\epsilon = 10^{-3}$). UF is performed for uniform cross-sectional inlet and outlet pressures P_{in} and $P_{out} = 1$ atm, respectively, and permeate pressure P_{perm} taken as constant. The above pressure boundary conditions are selected inside the operating window in Fig. 3 so that PFR and AFE are absent, except for two particular cases considered to elucidate their effects.

The solvent is water at room temperature, with viscosity $\eta_s = 10^{-3}$ Pa s. The hydraulic solvent permeability of the uniform membrane is selected as $L_P = 6.7\times10^{-10}$ m/(Pa s), which is a typical value in UF[2] used in Ref. 23. The associated dimensionless parameter k introduced in Eq. (26) is $k \approx 0.1464$.

The dispersed spherical particles are assumed to be monodisperse, with hard-core radius $a = 10$ nm and the single-particle diffusion coefficient $D_0(\gamma) = k_BT/(6\pi\eta_s\gamma a)$ equal to about 2.14×10^{-11} m^2/s for no-slip particles ($\gamma = 1$). The resulting radial Péclet number is $Pe_R \approx 78$ for no-slip spheres, corresponding to $\epsilon_\delta \approx 1.28\times10^{-2}$. The feed concentration at the fiber inlet is fixed to $\phi_b = 10^{-3}$.

We consider four different types of dispersions, as summarized in Table II. As a reference system, we use impermeable hard spheres (HS) where $\gamma = 1$, with the concentration dependence of

TABLE II. Discussed dispersion types. HS: impermeable hard spheres (reference system). PHS: solvent-permeable hard spheres where $\gamma < 1$. CT: fictitious hard-sphere system with constant transport properties D and η as indicated. CT0: like CT but for zero osmotic pressure Π.

Acronym	Π	D	η
HS	$\Pi(\phi)$	$D(\phi;\gamma=1)$	$\eta(\phi;\gamma=1)$
PHS	$\Pi(\phi)$	$D(\phi;\gamma<1)$	$\eta(\phi;\gamma<1)$
CT	$\Pi(\phi)$	$D(\phi_b)\approx D_0$	$\eta(\phi_b)\approx\eta_s$
CT0	0	$D(\phi_b)\approx D_0$	$\eta(\phi_b)\approx\eta_s$

the transport coefficients $D(\phi)$ and $\eta(\phi)$ and osmotic pressure $\Pi(\phi)$ accounted for using the analytic expressions in Sec. III. Dispersions of solvent-permeable hard particles (PHS) are described using the analytic transport coefficients in Sec. III for $\gamma < 1$ and the same osmotic pressure as for impermeable hard spheres. For permeable particles, values $0.763 \le \gamma < 1$ for the reduced hydrodynamics radius γ are considered. Using that $\kappa_p \approx a^2(1-\gamma)^2$ according to Eq. (16), this amounts to $\kappa_p \le 6$ nm^2 for the Darcy permeability of the particles. For comparison, the fixed value $L_P = 6.7 \times 10^{-10}$ m/(Pa s) corresponds to a Darcy permeability $\kappa \approx L_P\eta_s h \approx 235$ nm^2, where Eq. (13) and $h \approx R$ have been used. The Darcy permeability κ of the considered UF membrane is hence two orders of magnitude larger than the permeability of typical permeable colloidal particles. Even though $\kappa_p \ll \kappa$, according to Fig. 2, there is a significant dependence of the transport properties on κ_p.

To quantify the influence of the concentration dependence of D, η, and Π on the CP layer, we further analyze two fictitious systems (CT and CT0) where the transport coefficients are held constant, equal to their values at the inlet where $\phi = \phi_b$. In both systems, the flow is unperturbed by the CP layer. For system CT0, the osmotic pressure at the membrane wall is taken to be zero.

A. Pure solvent flow

We discuss first the velocity and pressure fields inside the membrane fiber for pure solvent flow where $\phi_b = 0$, as described by Eq. (31) for Stokes flow with $\epsilon Re \ll 1$, the small aspect ratio $\epsilon \ll 1$ and solvent recovery indicator $\beta^* \ll 1/\epsilon$. The operating conditions are selected such that unwarranted permeate flow reversal (PFR) and axial flow exhaustion (AFE) are avoided [cf. Fig. 3 and Eq. (33)], except for two explicitly noted cases. The employed values for $\Delta_L P$ are listed Table III, together with the resulting values for the base units $\alpha^* \approx \alpha$ and β^* and the solvent-recovery indicator β obtained using Eq. (31). AFE is observed for the lowest value $\Delta_L P = 30$ Pa (highest α^*) and PFR is observed for the highest value $\Delta_L P = 2 \times 10^4$ Pa (lowest α^*; cf. Fig. 3).

The flow profiles for the considered values of $\Delta_L P$ are shown in Fig. 5, where we demonstrate the quantitative agreement between analytic results based on Eq. (31) and FEM calculations (symbols).

In panels (a) and (b), the pressure and axial velocity distribution functions $\mathscr{P}(\tilde{z})$ and $\mathscr{U}(\tilde{z})$ are plotted, defined by

TABLE III. Values of the longitudinal pressure difference, $\Delta_L P$, used for the pure-solvent systems for fixed mean TMP $\Delta_T^{(l)} P = 5000$ Pa, $P_{out} = 1$ atm, and $k \approx 0.1464$. Additionally listed are resulting values for $\alpha^* = \Delta_T^{(l)} P/\Delta_L P$ and (linearized) solvent recovery indicator β (β^*).

$\Delta_L P$ (Pa)	α^*	β^*	β
30	1.67×10^2	3.57	1.28
53.4	9.36×10^1	2.01	1.00
10^2	5.00×10^1	1.07	6.96×10^{-1}
10^3	5.00	1.07×10^{-1}	1.01×10^{-1}
10^4	5.00×10^{-1}	1.07×10^{-2}	1.06×10^{-2}
2×10^4	2.50×10^{-1}	5.36×10^{-3}	5.32×10^{-3}

$$\mathscr{P}(\tilde{z}) = \frac{P(\tilde{z}) - P_{out}}{P_{in} - P_{out}}, \tag{53}$$

$$\mathscr{U}(\tilde{z}) = \frac{u(0,\tilde{z}) - u(0,1)}{u(0,0) - u(0,1)}, \tag{54}$$

respectively. These distribution functions are of values one at the inlet and zero at the outlet. The distribution function $\mathscr{U}(\tilde{z})$ quantifies the axial velocity along the center-line, $\tilde{r} = 0$, of the fiber. As it is expected, the axial deviations (convexity) of $\mathscr{P}(\tilde{z})$ from the linear Hagen–Poiseuille pressure drop $\mathscr{P}_{HP}(\tilde{z}) = 1 - \tilde{z}$ increases with decreasing $\Delta_L P$ (increasing β) due to enlarged solvent permeation into the permeate. For the smallest $\Delta_L P = 30$ Pa, axial flow exhaustion is observed for $\tilde{z} > \tilde{z}_{AFE} \approx 0.56$, where $\mathscr{P}$ becomes negative. The increase in $\mathscr{P}$ with increasing $\Delta_L P$ toward the linear HP profile is reflected in an according increase in the normalized axial velocity at the center-line, $u(\tilde{r}=0,\tilde{z})/u(0,0)$, depicted in the inset of panel (b). The curves for the axial velocity in the inset show stronger deviations from linearity when $\Delta_L P$ is larger. These (hyperbolic) nonlinearities are more visible in the axial velocity distribution function $\mathscr{U}(\tilde{z})$, which becomes more convex with increasing $\Delta_L P$. Here, permeate flow reversal is exhibited at axial distances $\tilde{z} > \tilde{z}_{PFR} \approx 0.50$ for the largest inlet-outlet pressure difference $\Delta_L P = 2 \times 10^4$ Pa. This is indicated by negative values of $\mathscr{U}(\tilde{z})$. Different from $\mathscr{P}(\tilde{z})$, $\mathscr{U}(\tilde{z})$ is undetermined for HP flow in a non-permeable pipe. Notice further that visible differences between FEM and analytic results for $\mathscr{U}(\tilde{z})$ are observed at $\Delta_L P = 2 \times 10^4$ Pa. In this case, it holds $\epsilon Re = 1.25$, meaning that the Stokes-flow condition $\epsilon Re \ll 1$ is not obeyed.

In bottom panels (c) and (d) of Fig. 5, we display the radial dependence of the reduced axial and radial velocity components $u(\tilde{r},\tilde{z})/u(0,\tilde{z})$ and $v(\tilde{r},\tilde{z})/v(1,\tilde{z})$, respectively. The zeroth-order in ϵ analytic flow solution in Eq. (31) has a factorized $\tilde{r}$ and $\tilde{z}$ dependence so that the reduced velocity components are equal to $\tilde{u}_R(\tilde{r})$ and $\tilde{v}_R(\tilde{r})$, respectively, whose expressions are quoted in the panels (c) and (d). There is again excellent agreement between analytic and FEM results also for the largest $\Delta_L P$. Owing to the cylindrical symmetry, the radial velocity in panel (d) attains its peak value inside the fiber at $\tilde{r} = \sqrt{2/3}$. As indicated by the dashed curve in this panel, this peak does not occur for a flat membrane where $\tilde{v}_R(\tilde{r})$ is changed to $\tilde{v}_R(\tilde{r}) = \left(3\tilde{r} - \tilde{r}^3\right)/2$, with maximal axial velocity attained

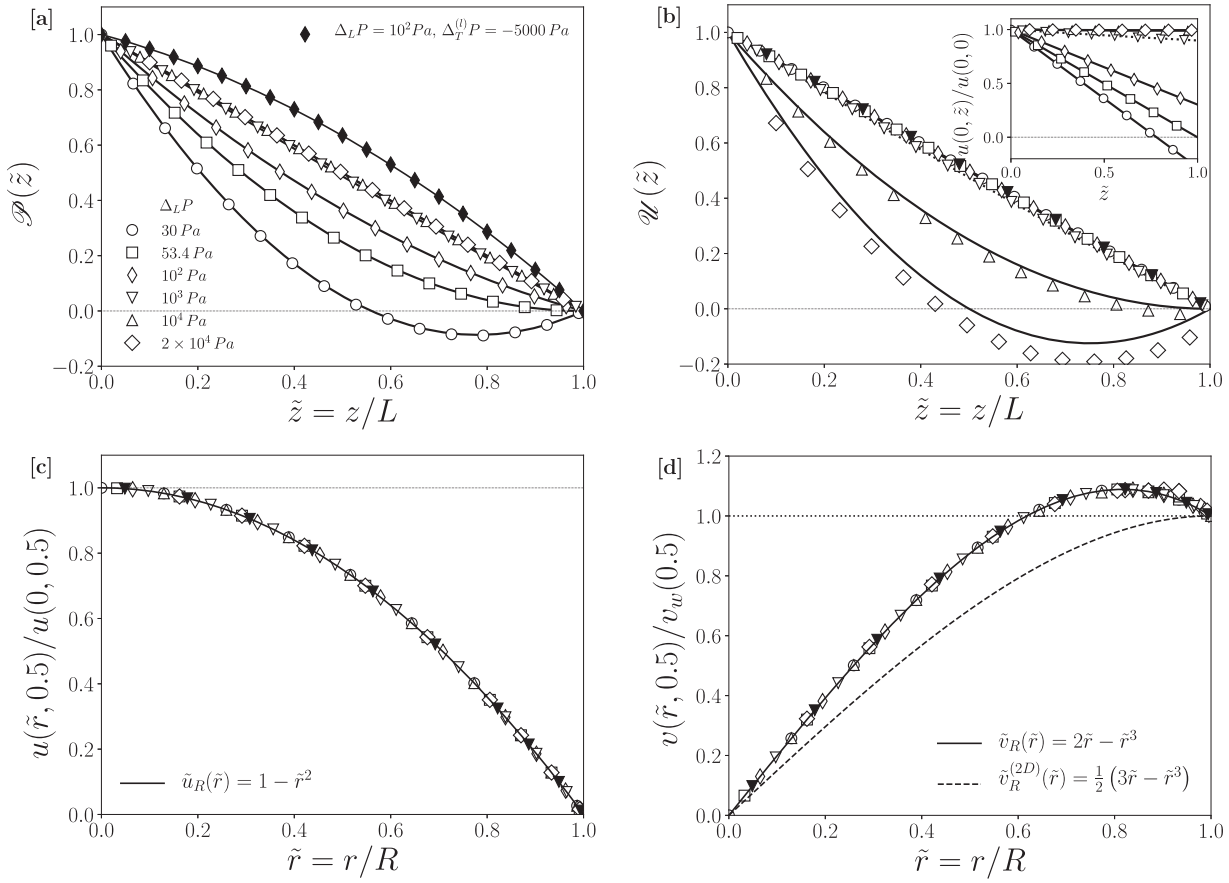

FIG. 5. Pure solvent flow profiles for various longitudinal pressure differences, $\Delta_L P$, as indicated. Curves are analytic and symbols are FEM calculation results. (a): Axial pressure distribution function $\mathscr{P}(\tilde{z})$ and (b): axial velocity distribution function, $\mathscr{U}(\tilde{z})$, at the fiber center. The inset in (b) shows the non-dimensionalized axial velocity $u(\tilde{r} = 0, \tilde{z})/u(\tilde{r} = 0, \tilde{z} = 0)$. (c) Normalized axial velocity and (d) normalized radial velocity as functions of $\tilde{r}$ viewed halfway along the fiber length at $\tilde{z} = 0.5$. The length-averaged linearized TMP is $\Delta_T^{(l)} P = 5000$ Pa and -5000 Pa for open and closed symbols, respectively.

at the membrane wall (see also the leading-order solutions in Refs. 8 and 9).

For completeness, we have included in Fig. 5 the reversed case (for $\Delta_L P = 10^3$ Pa only) where the permeate pressure is now larger than the inlet and outlet pressures, i.e., $P_{perm} > P_{in} > P_{out}$, with negative TMP, $\Delta_T^{(l)} P = -5000$ Pa (closed symbols). This case matters for outside-in UF setups and for the cleaning cycle in an inside-out setup. As shown in panel (a), a reversal from inside-out to outside-in permeation is indicated by a concave shape of $\mathscr{P}(\tilde{z})$. The good agreement between analytic and FEM results is observed also in this case.

B. Ultrafiltration of impermeable hard spheres

Having discussed the pure-solvent case, we address now UF of dispersions of solvent-impermeable hard spheres (HS) on assuming uniform cross-sectional feed concentration $\phi_b = \phi(r, z = 0) = 10^{-3}$ and dispersion properties D, η, and Π, as described in Sec. III for $\gamma = a_h/a = 1$. To analyze the influence of the concentration dependencies of dispersion properties on UF, we compare mBLA and FEM results with the according mBLA and FEM results for constant $D(\phi_b)$ and $\eta(\phi_b)$ taken at the feed concentration ϕ_b, while the concentration dependence of $\Pi(\phi)$ is preserved (system CT). In addition, we study the CT system specialized to zero osmotic pressure (i.e., system CT0 in Table II).

Figure 6 shows the volume concentration, $\phi_w(\tilde{z})$, of impermeable hard spheres at the membrane wall obtained using the semi-analytic mBLA (solid and dashed curves) and FEM (open symbols) methods. The mBLA and FEM results are compared with similarity solution (sBLA) predictions. The similarity solution was used in earlier works by Roa *et al.*[23] The influence of concentration-dependent suspension properties on UF is assessed by the comparison with respective results for systems CT and CT0 displayed in the inset.

There is quantitative agreement between FEM and mBLA data for both the HS and concentration-independent CT systems (see Table II). The viscosity increase in the CP layer due to an enlarged wall concentration is nearly counterbalanced by an associated increase in the gradient diffusion of particles away from

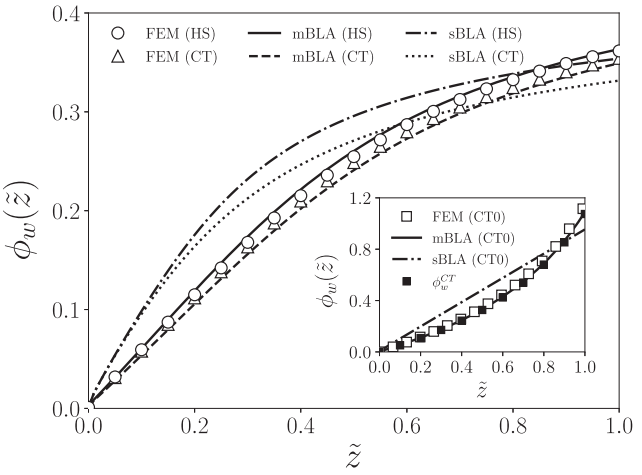

FIG. 6. Membrane wall concentration profile, $\phi_w(\tilde{z})$, for an impermeable hard-sphere (HS) dispersion. Open circles—FEM, solid curve—mBLA, and dashed–dotted curve—similarity solution (sBLA) results. For comparison, FEM (open triangles), mBLA (dashed curve), and sBLA (dotted curve) results are shown for constant $D(\phi_b)$ and $\eta(\phi_b)$. The inset includes FEM (open squares), mBLA (solid curve), and sBLA (dashed–dotted curve) results for system CT0 having constant transport properties and zero osmotic pressure. Closed squares are the prediction by the expression for ϕ_w^{CT} in Eq. (52), specialized to $\Pi = 0$. The operating conditions are $\Delta_L P = 130$ Pa and $\Delta_T^{(l)} P = 5000$ Pa, with $P_{out} = 1$ atm. The properties of the membrane and the HS and CT colloidal systems are described in the beginning of Sec. V (see also Table II).

the membrane wall. This explains why the CP layer wall concentration profile for concentration-dependent transport properties (HS case) is only slightly larger than that of the CT system. The largest concentration value $\phi_w(1) = 362 \times \phi_b$, observed at the outlet position $\tilde{z} = 1$, is still distinctly smaller than the freezing concentration $\phi_f = 0.494$ of hard spheres so that no reversible filter cake is formed. The inset in Fig. 6 demonstrates the outcome when the osmotic pressure Π is neglected in the generalized Darcy–Starling membrane law in Eq. (12). According to the FEM and mBLA results for the CT0 system, with the latter following from Eq. (52) for $\phi_w^{CT}(\tilde{z})$, the neglect of Π has two consequences for $\phi_w(\tilde{z})$, namely, a shape change in the concentration curve from concave to convex and a non-physically strong enhancement of $\phi_w(\tilde{z})$ to values above closest packing. This highlights the importance of the wall osmotic pressure in the UF of small particles executing strong Brownian motion, which, in our study, exert a thermal pressure $k_B T/V_a \approx 1000$ Pa comparable to $\Delta_T^{(l)} P$.

It is interesting to contrast, in Fig. 6, the mBLA results for $\phi_w(\tilde{z})$ with the similarity solution (sBLA) results based on the advection–diffusion equation for case AB given in Table I. The similarity solution was used already in earlier works on UF.[15,21–23] While it preserves the concave shape of ϕ_w for non-zero osmotic pressure, the similarity solution predicts a larger initial slope at the inlet. Furthermore, it distinctly overestimates the FEM concentration except for the outlet region where a cross-over of the sBLA and mBLA concentration curves is observed. For the CT0 system, the sBLA predicts a nearly linear increase in $\phi_w(\tilde{z})$, in distinct difference with the FEM/mBLA data.

We proceed by discussing the radial dependence of the CP layer volume concentration. Like for pressure and axial velocity, it is expedient to introduce a radial particle distribution function $\psi(\tilde{r},\tilde{z})$. For axial distances $z \gg L_D \sim L\epsilon_\delta^2$ sufficiently larger than the development length L_D, this function is defined by

$$\psi(\tilde{r},\tilde{z}) = \frac{\phi(\tilde{r},\tilde{z}) - \phi_b}{\phi_w(\tilde{z}) - \phi_b} \tag{55}$$

so that $\psi(\tilde{r} = 1, \tilde{z} > 0) = 1$ and $\psi(\tilde{r} = 0, \tilde{z} > 0) = 0$. Note that $\psi \approx 0$ holds in the bulk region outside the CP layer. In mBLA, the radial distribution function is obtained from the leading-order matched asymptotic solution as

$$\psi(\bar{y},\tilde{z}) = e^{-\bar{s}(\bar{y},\tilde{z})} - \frac{\phi_b}{\phi_w(\tilde{z}) - \phi_b}\bar{s}(\bar{y},\tilde{z})e^{-\bar{s}(\bar{y},\tilde{z})}, \tag{56}$$

where $\bar{y} = (1 - \tilde{r})/\epsilon_\delta$ is the stretched radial distance measured from the wall and $\bar{s}(\bar{y},\tilde{z})$ was introduced in Eq. (43). The non-negative function $\bar{s}(\bar{y},\tilde{z})$ is zero at the wall where $\bar{y} = 0$. Hence, mBLA predicts a single exponential decay of ψ with increasing wall distance $\bar{y}$ for the CT and CT0 systems, provided that for the considered $\tilde{z} > 0$, it holds that $\phi_w(\tilde{z}) \gg \phi_b$. For smaller wall concentrations, the second contribution $\bar{s}\exp\{-\bar{s}\}$ to ψ is non-negligible. For the general HS case with concentration-dependent dispersion properties, $\bar{s}/\bar{y}$ is non-constant and the decay of ψ is not single exponential in general. Note that $\bar{s}e^{-\bar{s}}$ goes to zero both for $\bar{y} \to 0$ and $\bar{y} \to \infty$, and it attains its maximum value of $1/e$ at $\bar{s} = 1$.

FEM and mBLA results for the radial particle distribution function $\psi(\tilde{r},\tilde{z})$ inside the CP layer are depicted in Fig. 7, as functions of $\bar{y}$, for constant transport properties (CT) in panel (a) and concentration-dependent transport properties (HS) in panel (b). Also regarding the radial concentration dependence, there is excellent agreement between FEM and mBLA for all distances $\tilde{z} > 0.1$. For system CT considered in panel (a), the decay of ψ with increasing wall distance is practically single exponential, as $\psi \approx \exp\{-\bar{s}\}$ according to mBLA. For later use, the inset shows $\bar{s}(\bar{y},\tilde{z})/\bar{y}$, which is independent of $\bar{y}$, as required for a single exponential decay of ψ.

Different from the CT case, the decay of ψ for the HS case in panel (b) is not single exponential any more, and ψ is larger at all axial distances $\tilde{z}$, which is mainly due to $D(\phi) > D(\phi_b)$. The non-exponential decay of ψ is reflected in a monotonically increasing $\bar{s}(\bar{y},\tilde{z})/\bar{y}$ shown in the inset, triggered by the monotonic increase in $D(\phi)$ with increasing ϕ, as depicted in Fig. 2(b). The monotonic behavior of $D(\phi)$ is characteristic for dispersions of Brownian particles with short-range repulsive direct interactions.[24] According to Eq. (43), in the CT case, it is $\bar{s}(\bar{y},\tilde{z})/\bar{y} \to \tilde{v}_w(\tilde{z})$ for $\bar{y} \to 0$, while in the HS case, the near-wall limit is approximately equal to $\tilde{v}_w(\tilde{z})/\tilde{D}(\phi_w) < \tilde{v}_w(\tilde{z})$.

From the knowledge of $\psi(\tilde{r},\tilde{z})$, one infers the mean thickness, $\delta(z)$, of the CP layer at axial distance z, defined by the cross-sectional average

$$\delta(z) = \frac{\int_0^R (R - r) r\, \psi(r,z)\, dr}{\int_0^R r\, \psi(r,z)\, dr}. \tag{57}$$

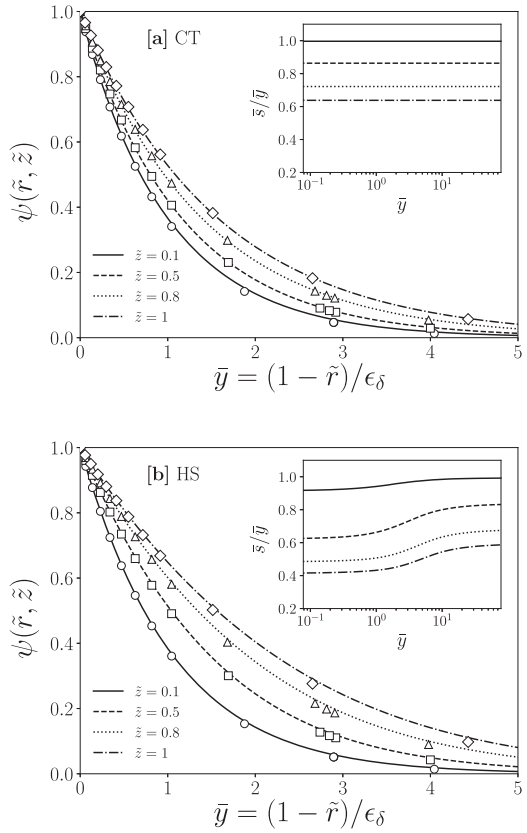

FIG. 7. Radial particle distribution function, $\psi(\tilde{r},\tilde{z})$, in the CP layer region as function of $\bar{y}$ for selected distances $\tilde{z}$ from the inlet as indicated. (a): FEM (open symbols) and mBLA (lines) results for constant transport (CT) properties and (b) for impermeable hard spheres concentration-dependent transport properties (HS). The insets in (a) and (b) depict the respective curves for $\bar{s}(\bar{y},\tilde{z})/\bar{y}$ as functions of $\bar{y}$. System parameters and operating conditions as in Fig. 6.

For system CT, an analytic expression for $\delta(z)$, named $\delta^{CT}(z)$, is obtained using Eq. (52) for ϕ_w^{CT} for axial distances $z \gg L_D$ where mBLA is valid. This expression reads

$$\frac{\delta^{CT}(z)}{\delta_{CP}} = \frac{\phi_w(z)[\tilde{v}_w(z) - 2\epsilon_\delta] - \phi_b[3\tilde{v}_w(z) - 8\epsilon_\delta]}{\tilde{v}_w(z)\phi_w(z) - \phi_b[2\tilde{v}_w(z) - 3\epsilon_\delta]} \frac{1}{\tilde{v}_w(z)}, \quad (58)$$

where $\delta_{CP} = \epsilon_\delta R$ is the characteristic thickness of the CP layer in Eq. (41). At axial positions where $\phi_w \gg \phi_b$, the expression reduces to $\delta^{CT}(z)/\delta_{CP} \approx 1/\tilde{v}_w(z)$.

The CP layer thickness $\delta(z)$ is shown in Fig. 8 for systems HS, CT, and CT0, obtained from FEM and mBLA calculations of $\psi(\tilde{r},\tilde{z})$, and compared with the analytic expression for $\delta^{CT}(z)$ in Eq. (58). For the CT0 system, $\delta(\tilde{z})$ is practically constant of value close to δ_{CP} at $\tilde{z} > 0.1$. This can be attributed to the near-constancy of the axially resolved reduced TMP, $[P(\tilde{z}) - P_{perm}]/\Delta_T^{(l)}P$, which varies only little from 1.016 at the inlet to 0.990 at the outlet, with an according permeate flux $\tilde{v}_w(\tilde{z})$, which is nearly constant.

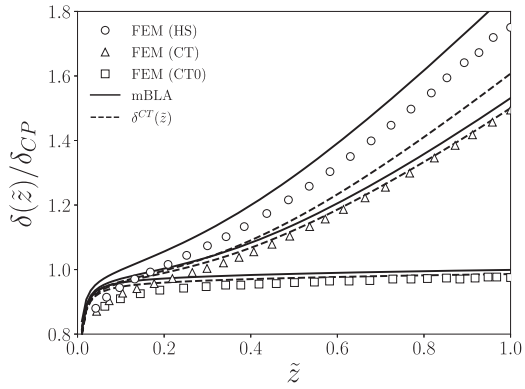

FIG. 8. Axially resolved mean CP layer thickness, $\delta(z)$, of the HS, CT, and CT0 systems obtained using FEM (symbols) and mBLA (solid lines). Additionally shown is $\delta(z)^{CT}$ according to Eq. (58), with $\tilde{v}_w(\tilde{z})$ determined using mBLA (dashed lines). The mean thickness is divided by $\delta_{CP} = D_0/v^* \approx 6.40 \times 10^{-6}$ m. System parameters and operating conditions as in Fig. 6.

We notice for the CT system that the concentration-dependent wall osmotic pressure gives rise to a monotonically increasing $\delta(z) \propto 1/\tilde{v}_w(z)$. The FEM data (open triangles) overlap with the corresponding dashed $\delta^{CT}(z)$ curve, while the solid mBLA curve is located slightly above the FEM data. As expected, $\delta(z)$ is further enlarged when the concentration dependence of D and η is accounted for (HS system). Here, the FEM data (open circles) are distinctly exceeded by the corresponding solid mBLA curve. Using in Eq. (58) the permeate flux $\tilde{v}_w(z;\phi_w(z))$ with $\phi_w(z)$ obtained from mBLA, the FEM data for the CP layer thickness are now underestimated (see the uppermost dashed curve). The pronounced differences between the mBLA and $\delta^{CT}(z)$ curves for the HS system are entirely due to the neglected concentration dependence of the transport coefficients in the latter curve. The concentration dependencies of D and η have the net effect to increase slightly the width $\delta(z)$ of the CP layer. This is essentially due to the influence of the gradient diffusion coefficient D, which increases with increasing concentration according to Eq. (18) and Appendix B. An increased D tends to spread out the diffuse CP layer. There is an additional contribution to the CP layer thickness due to the viscosity η, which, according to Fig. 2, also increases with increasing concentration. In overcompensating the gradient diffusion away from the membrane surface, the concentration-dependence of the viscosity of hard spheres causes a larger wall concentration profile $\phi_w(z)$, as noticed in Fig. 6 in comparison with the CT case.

So far, we have discussed the axial and radial variation of the CP concentration profile and the axial variation of its thickness. For the HS and CT systems, we analyze next the radial variation of the axial and radial velocity components u and v, respectively. According to the mBLA analysis, only u is affected by the CP layer.

Figure 9(a) includes results for the radial dependence of $u(\tilde{r},\tilde{z} = 0.5)$, normalized by its maximal value $u(\tilde{r} = 0,\tilde{z} = 0.5)$. In the bulk region of the lumen, the velocity profile is practically equal to the quadratic Hagen–Poiseuille (HP) profile inside

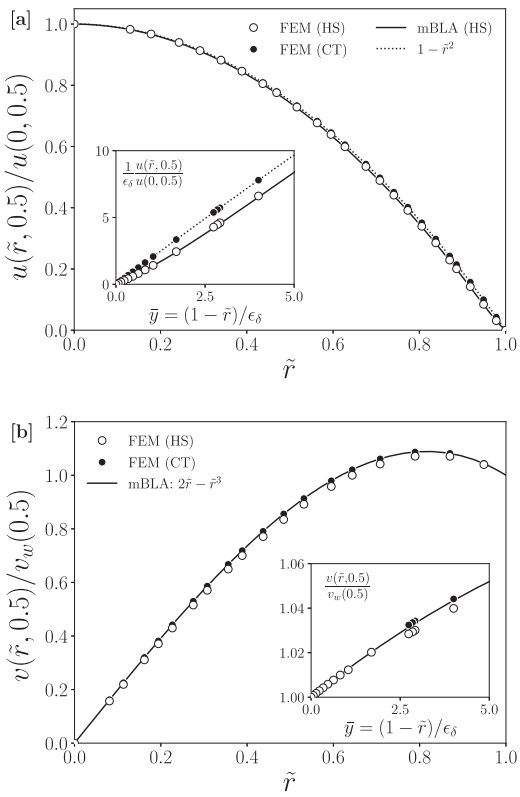

FIG. 9. Radial dependence of (a) normalized axial velocity, $u(\tilde{r},\tilde{z})$, and (b) normalized radial velocity, $v(\tilde{r},\tilde{z})$, of systems HS and CT evaluated halfway between the inlet and outlet. Insets in (a) and (b) show the respective velocity profiles in the CP layer region, with a stretching factor $1/\epsilon_\delta$ used in panel (a). Symbols are FEM data, solid curves are mBLA results, and the dotted curves in (a) are Hagen–Poiseuille predictions. System parameters and operating conditions as in Fig. 6.

a solvent-impermeable pipe for both the HS and CT systems. Deviations from the HP profile are manifested in the thin CP layer, as noticed in the inset where a linear increase in the stretched axial velocity with increasing (stretched) distance $\bar{y}$ from the membrane wall is observed. While for the CT system, the CP layer velocity profile is of the HP form (dotted line), in the HS model, the axial velocity (solid line) is perturbed away from the HP form, owing to the concentration dependence of $\eta(\phi)$. We observe again good agreement between FEM and mBLA results.

The radial dependence of the radial velocity component $v(\tilde{r},\tilde{z}=0.5)$ normalized by the permeate flux at $\tilde{z}=0.5$ is shown in Fig. 9(b). Its behavior in the CP layer region is resolved in the inset. The mBLA method predicts that $v(\tilde{r},\tilde{z})$ is equal to the pure-solvent form even inside the CP layer, given by $\tilde{v}_R = 2\tilde{r}-\tilde{r}^3$. The FEM data (symbols) are in accord with this polynomial behavior to an accuracy of $\mathcal{O}(\epsilon_\delta)$.

As noted in relation to the cross-sectional particle flux conservation law in Eq. (50), the dominant axial transport mechanism in UF is convection. It is useful to separate the axial (convective) flux $j(\tilde{r},\tilde{z})$ in Eq. (51) into its excess and bulk parts according to

$$j(\tilde{r},\tilde{z}) = (\phi-\phi_b)u + \phi_b u \equiv j_{ex} + j_b. \tag{59}$$

Note that without CP layer, j_{ex} is identically zero. Using this flux separation, the cross-sectionally integrated flux $\Phi(\tilde{z})$ in Eq. (50) is accordingly described as the sum of an excess and bulk part, i.e.,

$$\Phi(\tilde{z}) = \Phi_{ex}(\tilde{z}) + \Phi_b(\tilde{z}). \tag{60}$$

Figure 10 displays the excess and bulk axial flux contributions, $j_{ex}(\tilde{r},\tilde{z})$ and $j_b(\tilde{r},\tilde{z})$, calculated for an impermeable hard-sphere dispersion using FEM (symbols) and mBLA (lines). Notice the logarithmic scale for the reduced radial distance, $\tilde{y}$, from the membrane wall. The excess flux, j_{ex}, grows from zero at $\tilde{y}=0$ toward its maximal value at $\tilde{y}\sim\epsilon_\delta$, with a value of ϵ_δ marked by the dotted vertical line, with an ensuing decay of the excess flux toward its bulk value zero. The maximum of j_{ex} grows with increasing axial distance, $\tilde{z}$, from the inlet, and its position shifts to larger $\tilde{y}$. The radial position of the maximum can be used as an alternative measure of the thickness of the diffuse CP layer at a given $\tilde{z}$, resulting in values somewhat larger than those for $\delta(\tilde{z})$ defined in Eq. (57). The maximum of j_{ex} is a consequence of the trade-off between axial velocity u, which grows with increasing $\tilde{y}$, and excess concentration $\phi-\phi_b$, which decays to zero with increasing $\tilde{y}$. In comparison with the FEM results, mBLA tends to slightly overestimate the maximum for larger axial values $\tilde{z}$. Obviously, the reduced bulk flux, $j_b/(\phi_b u^*)=\tilde{u}$, increases monotonically from zero at $\tilde{y}=0$ to its maximum located at the pipe center $\tilde{y}=1$. Due to solvent leaking from the lumen into the permeate, the maximum of $\tilde{u}$ decreases with increasing $\tilde{z}$.

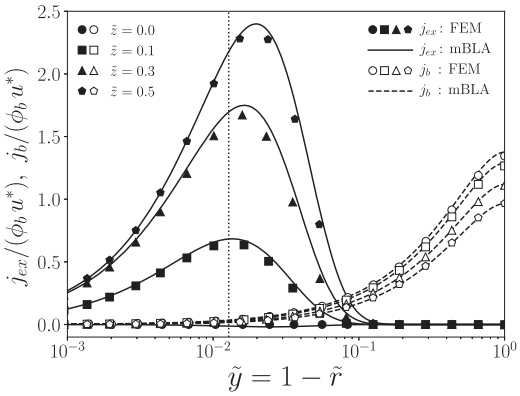

FIG. 10. Excess and bulk axial flux contributions, $j_{ex}(\tilde{r},\tilde{z})$ and $j_b(\tilde{r},\tilde{z})$, respectively, for the HS system, plotted as functions of the non-stretched reduced distance $\tilde{y}$ from the membrane, for axial positions $\tilde{z}$ as indicated. The fluxes are non-dimensionalized by division with $\phi_b u^*$. Closed and open symbols are FEM results for j_{ex} and j_b, respectively. Solid and dashed lines are associated mBLA results for j_{ex} and j_b, respectively. System parameters and operating conditions as in Fig. 6.

The described features of the axial flux contributions j_{ex} and j_b influence the behavior of the associated FEM and mBLA cross-sectional fluxes Φ_{ex} and Φ_b, which are plotted in Fig. 11. As shown in this figure, $\Phi_{ex}(\tilde{z})$ increases monotonically with increasing $\tilde{z}$ from 0 at the inlet to its maximal value at the outlet where the CP layer is the most pronounced. In contrast, $\Phi_b(\tilde{z})$ decays monotonically from its maximal value at the inlet to its minimal value at the outlet. According to the cross-sectional particle flux conservation law in Eq. (50), the sum $\Phi = \Phi_{ex} + \Phi_b$ is constant independent of $\tilde{z}$ for an ideally particle-retentive membrane. For the present operating conditions, Φ_b is larger than Φ_{ex} up to $\tilde{z} \approx 0.9$ where the two flux curves cross over. With increasing longitudinal pressure difference $\Delta_L P$, the crossover point shifts to larger $\tilde{z}$ and disappears eventually. Notice that for the considered cylindrical geometry, $\Phi_b(\tilde{z})$ is defined by a one-dimensional radial integral over $\tilde{r} j_b(\tilde{r}, \tilde{z})$, which puts more weight on flux contributions at larger radial distances $\tilde{r}$ from the pipe axis. Different from j_b, which has its maximum at $\tilde{r} = 0$, the maximum of $\tilde{r} j_b$ is shifted to $\tilde{r} \approx 1/\sqrt{3}$. The value $1/\sqrt{3}$ is exactly obtained for the CT system.

Up to this point, we have studied the concentration and flow profiles of impermeable hard-sphere dispersions for fixed operating conditions, namely, for $\Delta_L P = P_{in} - P_{out} = 130$ Pa and $\Delta_T^{(l)} P = 5000$ Pa with fixed $P_{out} = 1$ atm. In Fig. 12, we analyze how the wall concentration profile $\phi_w(\tilde{z})$ changes when the longitudinal pressure difference between the outlet and inlet is increased up to $\Delta_L P = 5000$ Pa. For increasing $\Delta_L P$, the outlet pressure is kept constant, equal to the atmospheric pressure, as assumed throughout this paper, while the values of P_{in} and P_{perm} are adjusted to comply with the considered $\Delta_L P$ value. All other UF parameters are the same as used before.

According to panel (a) of Fig. 12, the wall concentration profile flattens with increasing $\Delta_L P$, which is due to the enhanced axial convection of particles. For pressure differences $\Delta_L P > 1895$ Pa (i.e., $\alpha^* < 2.64$), the profile develops a maximum, which is shallow on the scale of panel (a). The non-monotonic behavior of $\phi_w(\tilde{z})$ at large $\Delta_L P$ is more clearly displayed on the adjusted scale of panel (b),

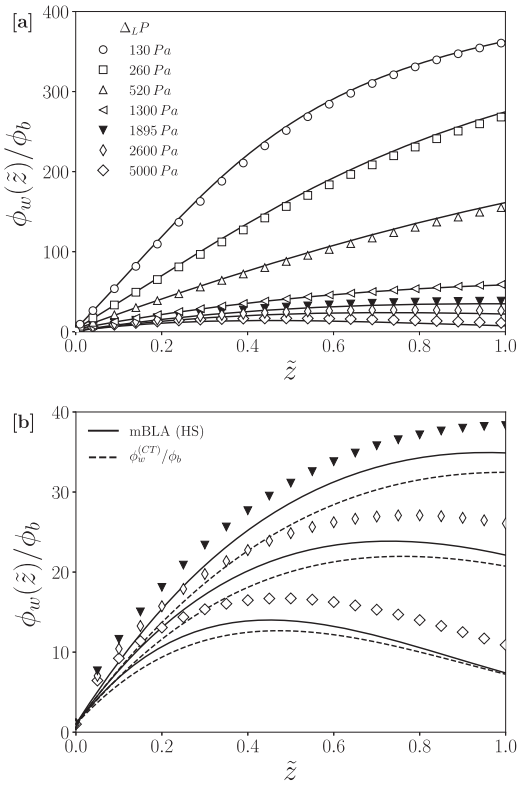

FIG. 12. (a) Normalized wall concentration profile, $\phi_w(\tilde{z})$, for increasing values of the longitudinal pressure difference $\Delta_L P$ as indicated. Symbols are FEM and solid lines are the respective mBLA results. In (b), the profiles for the three largest considered $\Delta_L P$ in (a) are magnified by using a different ordinate scale. The values for the ratio α^* of mean linearized TMP and $\Delta_L P$, corresponding to the $\Delta_L P$ values noted in (a), are $\alpha^* = \{38.46, 19.23, 9.62, 3.85, 2.64, 1.92, 1.00\}$, listed in the order of increasing $\Delta_L P$.

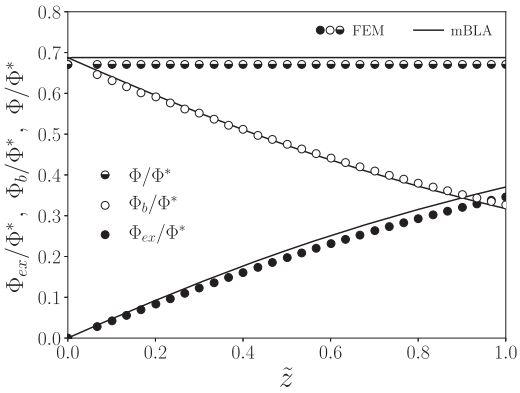

FIG. 11. Cross-sectional integrated excess and bulk axial flux contributions $\Phi_{ex}(\tilde{z})$ and $\Phi_b(\tilde{z})$, respectively, divided by their base unit $\Phi^* = \pi R^2 \phi_b u^*$. FEM (symbols) and mBLA (lines) results are shown for a HS system. The total cross-sectional flux, $\Phi = \Phi_{ex} + \Phi_b$, is constant. System parameters and operating conditions as in Fig. 6.

where also the shift of the maximum to smaller values of $\tilde{z}$ with increasing $\Delta_L P$ becomes visible. The relative difference between the FEM and mBLA data for ϕ_w increases according to the series {0.022, 0.031, 0.032, 0.025, 0.15, 0.17, 0.23} with accordingly increasing values of $\Delta_L P$ quoted in panel (a). Although the FEM concentration profile and particularly its maximum are somewhat underestimated by the mBLA result at large $\Delta_L P$ (solid lines), the overall shape and the location of the maximum are still well captured. The reason for the growing relative difference with increasing $\Delta_L P$ is that the condition $\phi_w \gg \phi_b$ in our leading-order boundary layer analysis is not strictly fulfilled any more for large $\Delta_L P$.

The dashed curves in panel (b) are the result by the analytic expression for $\phi_w^{CT}(\tilde{z})$ in Eq. (52) applied to the CT0 system. As seen, $\phi_w^{CT}(\tilde{z})$ provides a good qualitative description of the wall concentration profile for large $\Delta_L P$, where ϕ_w is small enough that the effects of the osmotic pressure and the concentration dependence of D and η are negligible.

We can further approximate $\phi_w^{CT}(\tilde{z})$ in Eq. (52) by its leading term in ϵ_δ given by

$$\frac{\phi_w^{CT}(\tilde{z})}{\phi_b} \approx 1 + \frac{\beta^*}{8\epsilon_\delta^2}\frac{\tilde{v}_w^2(\tilde{z})}{\tilde{u}_Z(\tilde{z})}\int_0^{\tilde{z}} \tilde{v}_w(\tilde{z}')d\tilde{z}'. \tag{61}$$

This expression allows for a crude approximation for the height of the profile maximum identified as $\beta^*/(8\epsilon_\delta^2) = \{43, 31, 16\}$ for the three $\Delta_L P$ values in panel (b).

To gain a physical understanding of the non-monotonic behavior of $\phi_w(\tilde{z})$, it is proficient to analyze first the simplified expression in Eq. (61). For large $\Delta_L P$, the pressure profile $\tilde{P}(\tilde{z}) \approx \tilde{P}_{in} - \tilde{z} \equiv \tilde{P}_{HP}(\tilde{z})$ is nearly equal to the linear HP pressure profile and $\tilde{u}_Z(\tilde{z})$ is nearly constant. For an illustration of these features, see Fig. 5(a) and the inset of Fig. 5(b). The permeate flux without osmotic pressure is, according to the Darcy–Starling equation, given by $\tilde{v}_w(\tilde{z}) = 1 + \alpha^*(1/2 - \tilde{z})$ when the linear HP pressure profile is used. This leads to a fourth-order polynomial in $\tilde{z}$ for the $\phi_w^{CT}(\tilde{z})$ in Eq. (61). For values $\alpha^* > 1/2$ inside the operating window in Fig. 3 and $0 < \tilde{z} \leq 1$, this polynomial predicts a unique maximum for ϕ_w^{CT}, provided that $\alpha^* < \alpha^*_{c,\max} = 2.91$, with a k-independent critical value $\alpha^*_{c,\max}$. The critical value is depicted by the horizontal dashed line in Fig. 13.

We perform next a more refined analysis based on the original expression for $\phi_w^{CT}(\tilde{z})$ in Eq. (52) without assuming a linear pressure profile. On physical grounds, we can identify numerically the critical value, $\alpha_c^*(k, \epsilon_\delta)$, of α^* using $d\phi_w^{CT}/d\tilde{z} = 0$ at $\tilde{z} = 1$ [cf. Fig. 12(b)]. Results for $\alpha_c^*(k, \epsilon_\delta)$ obtained from this numerical analysis using the NSolve function in Mathematica are shown in Fig. 13 as functions of k for different values of ϵ_δ as indicated. All results presented so far were obtained using $\epsilon_\delta = 1.28 \times 10^{-2}$ and $k = 0.1464$, which amounts to $\alpha_c^* = 2.64$ with corresponding $\Delta_L P = 1895$ Pa. The FEM and mBLA concentration profiles for this critical pressure difference are depicted in Fig. 12(b) (closed triangles). Notice that $k \sim \sqrt{\kappa}L/R^2$, with the Darcy permeability κ. Thus, k can be varied by changing the inner fiber radius R or κ, and $\epsilon_\delta = 1/Pe_R$ by changing the radial Péclet number. For given ϵ_δ, a non-monotonic concentration profile is predicted for all points (α^*, k) inside the according concave-shaped curve in Fig. 13. An interesting observation is that the curves for $\alpha_c^*(k, \epsilon_\delta)$ in Fig. 13 are bounded from above by $\alpha^*_{c,\max} = 2.91$. The upper boundary value is obtained for the linear HP pressure profile, while all the other depicted curves are based on convex-shaped pressure profiles (see Fig. 5).

In closing our discussion of Figs. 12 and 13, we remark that a non-monotonic profile for $\phi_w(\tilde{z})$ was observed also in earlier (long-time limiting) FEM-UF calculations by Marcos *et al.*,[29] but without deeper analysis. In that part of their results where ϕ_w is non-monotonic, they used $\Delta_T^{(l)}P = 27.6$ kPa and a characteristic wall shear rate of 8000/s, which translates into $\alpha^* \approx 1.07$. This value is well below the threshold value $\alpha_c^* = 2.54$ obtained using their parameters, showing the consistency of their findings with our analysis.

C. Ultrafiltration of permeable hard spheres

In this subsection, we study UF of dispersions of solvent-permeable Brownian hard spheres (PHS system in Table II). The viscosity $\eta(\phi; \gamma)$ and gradient diffusion coefficient $D(\phi; \gamma)$ of these dispersions are obtained using the analytic expressions in Sec. III based on the hydrodynamic radius model. Recall that $\gamma = a_h/a < 1$ is the reduced hydrodynamic radius, related by Eq. (16) to the reduced inverse hydrodynamic penetration depth by $\zeta \approx 1/\overline{\gamma} + \mathcal{O}(1/\overline{\gamma}^2)$, where $\overline{\gamma} = 1 - \gamma$. As illustrated in Figs. 2(a) and 2(b), an increasing permeability of the particles is reflected in a decreasing γ and hence in a decreasing viscosity and increasing gradient diffusion coefficient. The reduced hydrodynamic radii considered are $\gamma = \{1.0, 0.979, 0.888, 0.763\}$ corresponding to $\zeta = \{\infty, 50, 10, 5\}$. For zero permeability (HS system), $\gamma = 1$ and $\zeta = \infty$. For the osmotic pressure, we use again the Carnahan–Starling expression for hard spheres in Eq. (19), which is independent of γ.

Figure 14 quantifies the influence of solvent permeability on the wall concentration profile $\phi_w(\tilde{z})$. With increasing permeability (decreasing γ), the wall concentration decreases by about 30% for the smallest considered $\gamma = 0.763$ where the profile is nearly

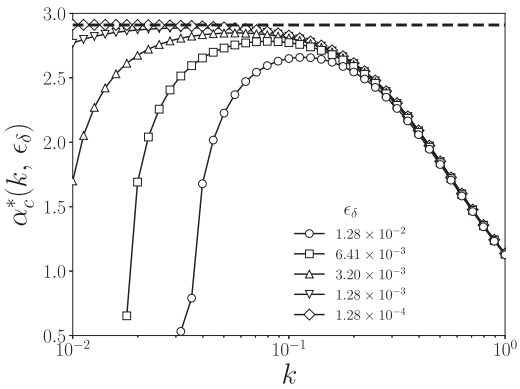

FIG. 13. Open symbols: mBLA predictions for the critical operating parameter $\alpha_c^*(k, \epsilon_\delta)$ for different ϵ_δ values as indicated. Solid lines are guides to the eye. The dashed horizontal line is $\alpha^*_{c,\max} = 2.91$. Non-monotonic wall concentration profiles are predicted for given k and ϵ_δ, provided that values for α^* are selected such that $\alpha^* < \alpha_c^*(k, \epsilon_\delta)$.

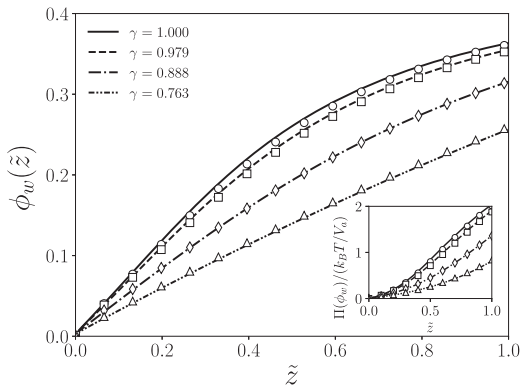

FIG. 14. Influence of solvent permeability on wall concentration profile, $\phi_w(\tilde{z})$, in the UF of permeable hard-sphere dispersions (PHS system) for values of reduced hydrodynamic radius γ as indicated. Open symbols are FEM and lines are mBLA results. The inset displays the osmotic wall pressure $\Pi(\phi_w(\tilde{z}))$ divided by the thermal pressure $k_BT/V_a \approx 1000$ Pa. Operating conditions are as in Fig. 6.

linear. Owing to the strictly monotonic behavior of the hard-sphere osmotic pressure in the fluid dispersion phase region, this feature of ϕ_w is reflected in the according wall osmotic pressure profiles displayed in the inset. According to Figs. 2(a) and 2(b), $D(\phi;\gamma)$ is enhanced with decreasing γ and the viscosity is lowered. The first effect enhances the particle diffusion out of the CP layer into the bulk, and the second one enhances cross-flow, which results in the combined effect that the CP layer is less strongly developed.

We analyze now how the solvent permeate flux is overall affected by the particle permeability. For this purpose, we investigate the so-called flow efficiency,

$$\frac{Q_{perm}}{Q^0_{perm}} = \frac{\Delta_T P - \langle \Pi \rangle}{\Delta^0_T P} \approx 1 - \frac{\langle \Pi \rangle}{\Delta_T P} < 1, \tag{62}$$

where

$$\langle \Pi \rangle = \frac{1}{L} \int_0^L dz \left[\Pi(\phi_w(z)) - \Pi_{perm} \right] \tag{63}$$

is the fiber length-averaged trans-membrane osmotic pressure, with the permeate osmotic pressure Π_{perm} taken to be zero throughout this work. The permeate volume flow rate of solvent through the particle-retentive membrane, Q_{perm}, was defined already in Eq. (25). Here, $Q^0_{perm} = 2\pi R L L_P \Delta^0_T P$ is its expression for the pure solvent case, and $\Delta^0_T P$ is the according fiber length-averaged TMP. According to Fig. 15, the flow efficiency decreases with increasing TMP. This decrease is less pronounced for permeable particles due to a less developed CP layer with the accordingly reduced wall osmotic pressure. The latter counteracts the TMP in the Darcy–Starling law in Eq. (12) for the permeate flux. Since $k = 0.1464$ is small, we obtain $\Delta^0_T P \approx \Delta_T P \approx \Delta^{(l)}_T P$, where $\Delta^{(l)}_T P$ is the length-averaged, linearized TMP introduced in Eq. (8). The inset in Fig. 15 shows the ratio, $\langle \Pi \rangle / \Delta_T P$, of length-averaged osmotic pressure and TMP, which, according to the right-most approximate equation in Eq. (62), determines the flow efficiency accurately. The key point to remember from Fig. 15 is that the reduction in flow efficiency is practically due to the osmotic pressure alone, since for small k, the convex deviation from linearity of the pressure profile $P(z)$ is very small [cf. also Eq. (34) for small k].

We finally investigate how the radial dependencies of the particle volume concentration and excess axial flux are affected by the solvent permeability of particles. Based on the matched asymptotic solution for $\phi(\tilde{y},\tilde{z})$ in Eq. (49), we use here a simplified and more qualitative analysis by ignoring the axial variations of the concentration and flow inside the CP layer. Explicitly, in Eq. (49), we substitute the $\tilde{z}$-independent values $\phi_w = 0.4$, $\tilde{v}_w = 1$, and $\tilde{u}_Z = 1$. For the

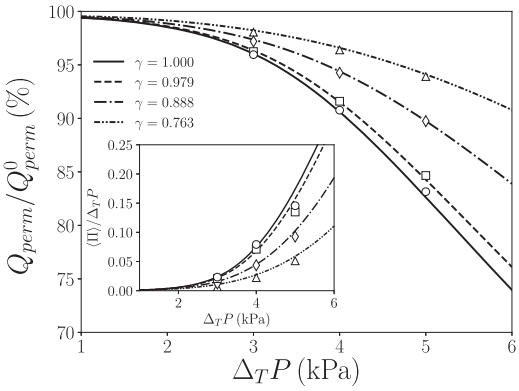

FIG. 15. Solvent flow efficiency, Q_{perm}/Q^0_{perm}, calculated using FEM (open symbols) and mBLA (lines) for reduced hydrodynamic radius values γ as indicated. The inset depicts the length-averaged wall osmotic pressure, $\langle \Pi \rangle$, divided by the length-averaged TMP $\Delta_T P$ and plotted vs $\Delta_T P$. System parameters and operating conditions as in Fig. 14.

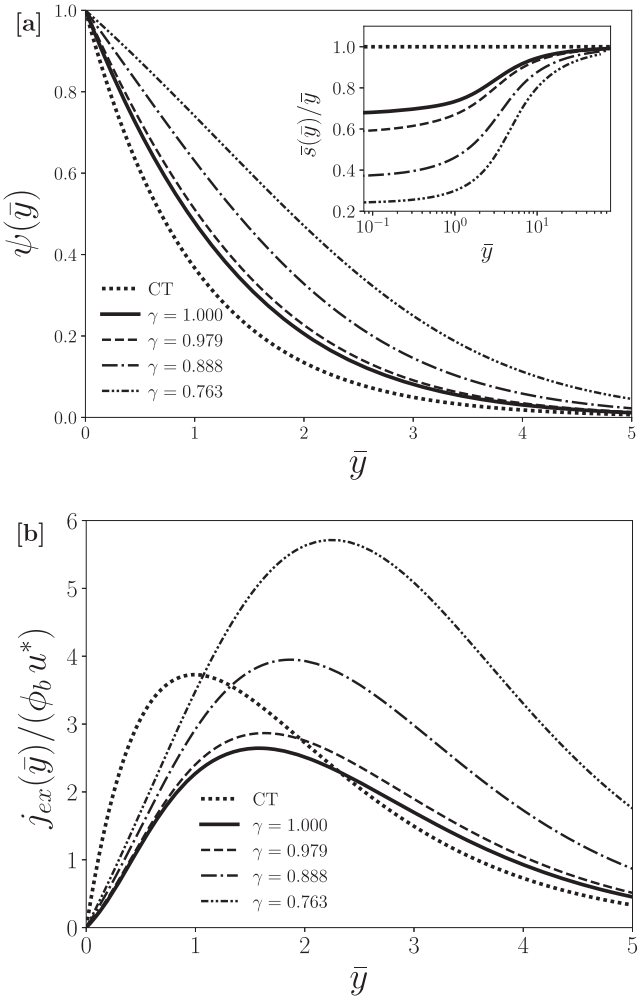

FIG. 16. (a) Estimated radial particle distribution function $\psi(\tilde{y})$ and (b) non-dimensionalized excess particle flux $j_{ex}(\tilde{y})/(u^*\phi_b)$ obtained from the matched asymptotic solution in Eq. (49) for given values $\phi_w = 0.4$, $\tilde{v}_w = 1$, and $\tilde{u}_Z = 1$ taken as $\tilde{z}$-independent. For the PHS system, various values of γ are considered as indicated. Dotted lines are the according prediction for the CT system. Other system parameters and operating conditions as in Fig. 6.

considered large wall concentration where $\phi_w/\phi_b = 400$, the matched solution reduces further to $\phi(\bar{y}) \approx \phi_w \exp\{-\bar{s}(\bar{y})\}$.

The resulting estimate for the $\bar{y}$-dependence of the radial particle distribution function, $\psi(\bar{y})$, is presented in Fig. 16(a) for various γ, together with the $\bar{y}$-normalized function $\bar{s}(\bar{y})/\bar{y}$ (inset). The function $\bar{s}(\bar{y})$ appears as exponent in the matched asymptotic solution for the volume concentration in Eq. (49). A single-exponential radial decay of $\phi(\bar{y})$ is observed for the CT system, as reflected by the accordingly constant $\bar{s}/\bar{y}$ shown as the dotted line in the inset. For this system, $\tilde{D} \approx 1$, $\tilde{\eta} \approx 1$, and $\Pi(0.4) = 2.77 \times k_B T/V_a$. Significant deviations from the single-exponential radial decay are observed already for a HS system of impermeable particles where $\gamma = 1$. The non-exponential slower decay of $\psi(\bar{y})$ becomes further enhanced with increasing permeability (see the inset), reflected in a more extended CP layer. It should be recalled that we have enforced a fixed value for ϕ_w, whereas γ is varied.

Figure 16(b) shows the radial dependence of the associated reduced excess axial flux, $j_{ex}(\bar{y})/(\phi_b u^*)$. With increasing permeability (decreasing γ), the excess flux is enhanced, and it spreads out to larger distances $\bar{y}$ from the membrane wall, consistent with the behavior of $\psi(\bar{y})$ in panel (a). The differences in the excess flux between systems CT (dotted line) and HS (solid line) are due to the disregard of concentration-dependent viscosity effects in the former system on the stretched axial velocity $\tilde{u} = \tilde{u}/\epsilon_\delta$ [see also the inset of Fig. 9(a)].

VI. CONCLUSIONS

We have presented a generic model describing CP layer effects in the cross-flow ultrafiltration (UF) of dispersions of solvent-permeable, hard spherical particles inside a hollow fiber membrane. To this end, we derived a versatile semi-analytic modified boundary layer approximation (mBLA) method of calculating axial and radial concentration and flow profiles. In addition, global UF quantities were analyzed, including the mean CP layer thickness, cross-sectionally integrated excess and bulk fluxes, and the solvent flow efficiency. The quantitative accuracy of the mBLA method was assessed by the comparison with elaborate FEM calculations for the same systems. We showed by this comparison that the mBLA method gives more accurate results for the concentration field than a boundary layer similarity solution used in earlier works. In this way, we have established the mBLA method as an efficient, accurate, and versatile method of predicting UF concentration and flow properties. Another benefit of this method is that it inter-relates concentration and flow properties with the hydrodynamic structure (i.e., solvent permeability) of the dispersed particles.

For the concentration- and permeability-dependent viscosity and gradient diffusion coefficient entering into the UF equations, we used accurate analytic expressions, which are well tested against dynamic computer simulations. The concentration-dependent effects of these transport properties and the osmotic pressure were examined by the juxtaposition with results by the schematic CT and CT0 systems where the transport properties are kept constant. Using the mBLA method, explicit analytic expressions were derived for the CT(0) systems concentration and flow profiles. These expressions are also useful for identifying general trends and unexpected features such as the non-monotonic wall concentration profile $\phi_w(\tilde{z})$ observed for strong axial convection (cf. Figs. 12 and 13). On the basis of the CT0 system, we were able to derive a criterion (i.e., a critical operating parameter α_c^*) for the occurrence of non-monotonic concentration profiles.

Moreover, criteria have been provided in Eq. (33), which allow for identifying the values for the characteristic operating parameter α^* where unwarranted axial flow exhaustion (AFE) and permeate flow reversal (PFR) are absent. While derived for the pure-solvent case, these criteria are likewise valid for the UF of dispersions described by the mBLA method.

The presented semi-analytic mBLA method, in conjunction with the accurate descriptions of transport properties of solvent-permeable particles, can be useful for the design, analysis, and optimization of UF setups. The present paper bridges the gap between fundamental properties of colloidal particles with internal hydrodynamic structure and the UF process of industrial and medical relevance. It gives new insight into the transport mechanisms pertinent to the UF process.

An intriguing result included in Fig. 10 is the assessment of the radial extension of the excess axial flux j_{ex} and the dependence of excess and bulk fluxes on the axial distance from the inlet. The figure highlights that the (diffuse) region wherein j_{ex} is different from zero extends significantly beyond the characteristic CP layer thickness δ_{CP}. The excess flux in this region increases strongly with increasing ϕ_w.

Two radial curvature effects due to the cylindrical geometry of the membrane are, first, the maximum of the radial velocity v away from the membrane wall at $r = \sqrt{2/3}R$ and, second, a cross-sectionally integrated axial flux $\Phi_{ex}(\tilde{z})$ distinctively larger than in a planar membrane geometry.

The solvent permeability of particles increases gradient diffusion and lowers the dispersion viscosity. These features cause the suppression of the strength of the CP layer and an according increase in the solvent flow efficiency. For the solvent permeability to be influential in UF, the wall concentration should be large and the hydrodynamic radius should be sufficiently smaller than the hard-core particle radius.

In our generic study of CP layer effects, we have disregarded fouling effects such as filter cake formation, adsorption of particles at the membrane, and the clogging of membrane pores. These are specific phenomena depending on the properties (e.g., morphology) of the membrane and material-specific properties of the particles and solvent. For the operating conditions used in this paper, there is no reversible cake formation by crystallization or vitrification. Following earlier works by Bacchin *et al.*,[36,37] reversible filter-cake formation can be included into the present mBLA method by using an extended Darcy–Starling equation where the additional hydraulic cake resistance is accounted for, in conjunction with assuming a constant volume fraction (e.g., freezing transition) value at the interface of cake and CP layers.

The present mBLA method assumes mono-disperse particles. Polydispersity can be included by accounting for cross correlations in the hydrodynamic mobilities and diffusivities, which gives rise

to a system of advection–diffusion equations where the concentrations and fluxes of the various components are coupled. Size polydispersity enlarges the concentration in the CP and cake layers and enhances clogging and, in combination with axial convection, the tendency of size-fractionation along the membrane fiber.

Additional features, disregarded in our UF treatment, are patterned membranes consisting of alternating particle-permeable and impermeable segments and UF effects caused by this patterning. An exploration of cake layer effects, polydispersity, UF of microgel suspensions, and patterned membranes based on accordingly extended mBLA methods will be the topic of future works.

ACKNOWLEDGMENTS

The authors gratefully acknowledge E. Zholkovskiy (Ukrainian Academy of Sciences) and M. Brito and J.K.G. Dhont (Forschungszentrum Jülich) for helpful discussions. This work was under appropriation of funds from the Deutsche Forschungsgemeinschaft (SFB-985, Project B6).

APPENDIX A: FINITE-ELEMENT METHOD (FEM)

Using the *Laminar Flow* and *Transport of dilute Species* packages of COMSOL, we have obtained numerically the weak axisymmetric two-dimensional solutions of the flow and concentration fields of the effective Stokes and time-dependent advection–diffusion Eqs. (2)–(4), respectively, coupled through the Darcy–Starling law and the reflective wall boundary condition for operating conditions described in Sec. II. While we are interested in steady-state results, for improved numerical stability, the time-dependent advection–diffusion Eq. (2) is solved using zero-flow and uniform pressure initial boundary conditions, starting from a tube initially filled with the solvent only, for time independent uniform volume fraction ϕ_b of particles at the inlet lumen cross section. Different from the semi-analytic boundary layer analysis, axial diffusion is accounted for in the FEM calculations, which, however, is small compared with axial convection. We use a backward-differentiation method for the time stepping. The steady-state solutions are monitored once transients in the flow and concentration profiles have decayed, typically after the characteristic time $t \sim 10 \times R^2/D_0$. As pressure operating conditions, we specify the values of $\Delta_L P$ and $\Delta_T^{(l)} P$ discussed in Sec. II. The employed analytic expressions for the gradient diffusion coefficient D, low-shear viscosity η, and osmotic pressure Π are summarized in Sec. III.

Streamline and crosswind stabilizations are invoked for both the Stokes equation (P1/P1 elements) and the advection–diffusion equation (P2 element). We use triangular and quadrilateral meshes in the bulk and the boundary (CP) layer regions, respectively, with the meshes generated by COMSOL. The smallest radial thickness of the mesh near the inner membrane wall is about $10^{-3}R$. This is sufficiently small to capture the radial flow and concentration variations in the CP layer region, since for the operating conditions reported in the result Sec. V, the element Péclet number[38] is smaller than one. For computational efficiency, the radial thickness of the near-wall quadrilateral mesh part is increasing, with a constant growth rate, in directions away from the membrane wall. The axial mesh thickness is stretched by a factor of 100 relative to the radial thickness, since $L/R = 1000$ is very large. A similar mesh generation is described in Refs. 29 and 39 where, however, triangular elements are used in both the bulk and boundary layer regions of the lumen.

APPENDIX B: SOLVENT-PERMEABLE PARTICLE TRANSPORT PROPERTIES

We provide here the analytic expressions for the low-shear-rate viscosity $\eta(\phi;\gamma)$, the equilibrium gradient diffusion coefficient $D(\phi;\gamma)$, and the osmotic compressibility factor $S(\phi)$ for dispersions of solvent-permeable colloidal hard spheres.[25]

We employ an expression for the high-frequency viscosity part η_∞ in Eq. (17) given by

$$\frac{\eta_\infty(\phi;\gamma)}{\eta_s} = 1 + \frac{5}{2}\gamma^3\phi\frac{1+\phi\widehat{S}(\gamma)}{1-\gamma^3\phi\left[1+\phi\widehat{S}(\gamma)\right]}, \tag{B1}$$

with the generalized Saito function

$$\widehat{S}(\gamma) = \left[\frac{2\lambda_V(\gamma)}{5\gamma^3} - \gamma^3\right], \tag{B2}$$

where

$$\lambda_V(\gamma) = 5.0021 - 39.279\bar{\gamma} + 143.179\bar{\gamma}^2 - 288.202\bar{\gamma}^3 + 254.581\bar{\gamma}^4, \tag{B3}$$

and $\bar{\gamma} = 1 - \gamma$.

The analytic expression for the shear relaxation viscosity part $\Delta\eta$ in Eq. (17) is

$$\Delta\eta(\phi;\gamma) = \frac{\eta_\infty(\phi;\gamma)}{\Gamma_S(\phi;\gamma)}\frac{\Delta\eta^{(no-HI)}(\phi)}{\eta_s}, \tag{B4}$$

where $\Delta\eta^{(no-HI)}(\phi)$ is the expression for $\Delta\eta$ without hydrodynamic interactions equal to

$$\frac{\Delta\eta^{(no-HI)}(\phi)}{\eta_s} \approx \frac{12}{5}\frac{\phi^2\left(1-7.085\phi+20.182\phi^2\right)}{1-\phi/0.64}. \tag{B5}$$

Here, $\Gamma_S(\phi;\gamma)$ is a short-time generalized Stokes–Einstein function, which reads

$$\Gamma_s(\phi;\gamma) = \frac{D_S(\phi;\gamma)}{D_0(\gamma)}\frac{\eta_\infty(\phi;\gamma)}{\eta_s}. \tag{B6}$$

Furthermore,

$$\frac{D_s(\phi;\gamma)}{D_0(\gamma)} = 1 + \lambda_t(\gamma)\phi\left[1+0.12\phi-0.70\phi^2\right] \tag{B7}$$

with

$$\lambda_t(\gamma) = -1.8315 + 7.820\bar{\gamma} - 14.231\bar{\gamma}^2 + 14.908\bar{\gamma}^3 - 9.383\bar{\gamma}^4 + 2.717\bar{\gamma}^5 \tag{B8}$$

is the short-time self-diffusion coefficient $D_s(\phi;\gamma)$, divided by its infinite dilution value $D_0(\gamma) = k_BT/(6\pi\eta_s a\gamma)$.

On the right-hand side of the gradient diffusion coefficient expression in Eq. (18), we use the Carnahan–Starling osmotic compressibility factor for hard spheres,

$$S(\phi) = \frac{(1-\phi)^4}{(1+2\phi)^2 + \phi^3(\phi-4)}, \tag{B9}$$

and the (short-time) sedimentation coefficient

$$K(\phi,\gamma) = 1 + \lambda_K(\gamma)\phi\left[1 - 3.348\gamma\phi + 7.426(\gamma\phi)^2 - 10.034(\gamma\phi)^3 + 5.882(\gamma\phi)^4\right], \tag{B10}$$

where

$$\lambda_K(\gamma) = -6.5464 + 8.592\tilde{\gamma} - 3.901\tilde{\gamma}^2 + 2.011\tilde{\gamma}^3 - 0.142\tilde{\gamma}^4. \tag{B11}$$

APPENDIX C: ASYMPTOTIC MATCHING

We explain here the asymptotic matching of the leading-order inner and outer solutions for the axial velocity u and the volume concentration ϕ given in Sec. IV B. As discussed therein, no asymptotic matching is required to leading order for the pressure P and the radial velocity v.

From equating the outer representation of the inner velocity solution,

$$\tilde{u}^{in}(\tilde{y}\to\infty,\tilde{z}) = c(\tilde{z})\,2\tilde{y}, \tag{C1}$$

to the inner representation of the outer solution,

$$\tilde{u}^{out}(\tilde{y}\to 0,\tilde{z}) = \tilde{u}_Z^{out}(\tilde{z})\,2\tilde{y}, \tag{C2}$$

we can identify the tangential dispersion stress at the membrane, equal to $2\,c(\tilde{z})$, as $c(\tilde{z}) = \tilde{u}_Z^{out}(\tilde{z})$. For simplicity, we use here the multiplicative mixing rule[40] for the matched axial velocity $\tilde{u}$, i.e.,

$$\tilde{u}(\tilde{y},\tilde{z},[\phi_w]) = \frac{\tilde{u}^{in}\tilde{u}^{out}}{2\tilde{u}_Z^{out}\tilde{y}} = \tilde{u}_Z^{out}(2-\tilde{y})\int_0^{\tilde{y}}\frac{1}{\tilde{\eta}}\frac{d\tilde{y}'}{\epsilon_\delta}, \tag{C3}$$

where the product of inner and outer solution has been divided by the common (overlap) part $2\tilde{u}_Z^{out}\tilde{y}$. Using $2-\tilde{y} = 1+\check{r}$, this gives Eq. (49).

For the matched volume concentration ϕ, we use an additive mixing rule

$$\phi(\tilde{y},\tilde{z}) = \phi^{in}(\tilde{y},\tilde{z}) + \phi^{out} - \phi'(\tilde{y},\tilde{z}), \tag{C4}$$

with $\phi^{out} = \phi_b$ and $\phi^{in} = \phi_w e^{-\tilde{s}}$. The so far unknown correction function ϕ' is determined next from using the three conditions

$$\lim_{\tilde{y}\to 0}\phi' = \phi_b, \quad \lim_{\tilde{y}\to\infty}\phi' = 0, \quad \text{and} \quad \lim_{\tilde{y}\to 0}\frac{\partial\phi'}{\partial\tilde{y}} = 0, \tag{C5}$$

where the third one imposes the zero normal flux condition at the membrane wall [see Eq. (9)].

The expression

$$\phi'(\tilde{y},\tilde{z},[\phi_w]) = \phi_b e^{-\tilde{s}(\tilde{y},\tilde{z},[\phi_w])}\left(1+\tilde{s}(\tilde{y},\tilde{z},[\phi_w])\right) \tag{C6}$$

satisfies these three conditions exactly. In addition, the resulting matched ϕ in Eq. (49) is a solution both of the zeroth-order inner and outer advection–diffusion equations. The extra term, $\tilde{s}e^{-\tilde{s}}$, in ϕ' guarantees the exact validity of the zero-flux boundary condition regarding ϕ, and it is related to the first-order in ϵ_δ singular perturbation correction. While this extra term is negligible for $\phi_b/\phi_w \lesssim \mathcal{O}(\epsilon_\delta)$, in accord with $\phi(\tilde{y},0) = \phi_b[1+\mathcal{O}(\epsilon_\delta)]$, it significantly improves the agreement with FEM calculation results when ϕ_b/ϕ_w is not small.

APPENDIX D: DETERMINATION OF ϕ_w

In this the appendix, we describe how the particle concentration profile at the membrane wall, $\phi_w(\tilde{z})$, is determined numerically using a fixed-point iteration (FPI) method based on the particle-flux conservation law in Eq. (50). We further show how the approximate analytic expression in Eq. (52) for the wall concentration is obtained for constant $D = D_0$ and $\eta = \eta_s$ and zero osmotic pressure.

We start by defining the linear integral operator $T_{\tilde{z}'}$ acting on functions $f(\check{r},\tilde{z})$ by

$$T_{\tilde{z}'}[f] = \tilde{u}_Z^{out}(\tilde{z}',[\phi_w])\int_0^1 \check{r}(1+\check{r}) \times\left(\int_{\check{r}}^1 \frac{1}{\eta(\phi(\check{r}',\tilde{z}',[\phi_w]))}d\check{r}'\right) f(\check{r},\tilde{z}=\tilde{z}')\,d\check{r}. \tag{D1}$$

Note that $T_{\tilde{z}'}$ is functionally dependent on ϕ_w.

From substituting the matched asymptotic solutions for ϕ and $\tilde{u}$ into Eq. (50), one realizes that the particle flux conservation law can be expressed in terms of the radial integral operator as

$$T_{\tilde{z}}[\phi] = T_0[\phi]. \tag{D2}$$

Substituting the matched asymptotic solution $f=\phi$ into this operator equation gives an implicit integral equation for ϕ_w,

$$\frac{\phi_w}{\phi_b} = 1 + \frac{T_0\left[1-\tilde{s}e^{-\tilde{s}}\right] - T_{\tilde{z}}\left[1-\tilde{s}e^{-\tilde{s}}\right]}{T_{\tilde{z}}\left[e^{-\tilde{s}}\right]} \equiv F_{\tilde{z}}[\phi_w], \tag{D3}$$

which defines the non-linear operator $F_{\tilde{z}}$. Note here that $\tilde{s} = \tilde{s}(\check{r},\tilde{z},[\phi_w])$ is a functional of ϕ_w and that $F_{\tilde{z}}$ is operating on $\tilde{s}$ taken at axial distance $\tilde{z}$ from the inlet.

To solve the implicit integral Eq. (D3) for $\phi_w(\tilde{z})$, we use the under-relaxed fixed-point iteration (FPI) scheme,[41]

$$\phi_w^{(n+1)}(\tilde{z}) = (1-w)\phi_w^{(n)} + w\,\phi_b\,F_{\tilde{z}}\left[\phi_w^{(n)}\right], \tag{D4}$$

for $\tilde{z}\in(0,1]$ and relaxation parameter $0<w\le 1$. With the wall concentration profile $\phi_w(\tilde{z})$ calculated in this way, the matched asymptotic solution for $\phi(r,z)$ in Eq. (49) and the flow field are fully determined.

We have commonly used the uniform starting profile $\phi_w^{(0)}(\tilde{z}) = \phi_b$ in the FPI, but we checked that the result for ϕ_w is insensitive to the uniform starting values $\phi_w^{(0)}$, selected to be

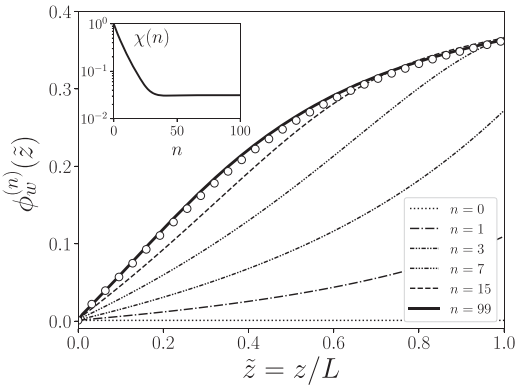

FIG. 17. Particle wall volume concentration iterations, $\phi_w^{(n)}(\tilde{z})$, for increasing iteration number n as indicated (curves) and compared with the FEM result (open circles) for $\phi_w(\tilde{z})$. The inset shows the relative difference, $\chi(n)$, according to Eq. (D5). The considered dispersion is an aqueous impermeable hard-sphere system with $\phi_b = 10^{-3}$. The membrane is characterized by $k \approx 0.1464$, and the UF operating conditions are $\Delta_T^{(l)} P = 5\,kPa$ and $\Delta_L P = 130$ Pa.

smaller than the freezing transition value $\phi_f = 0.494$ of colloidal hard spheres. The optimal choice of the relaxation parameter w depends, in principle, on the operating conditions and dispersion properties. We found $w = 0.1$ to be a good selection for all systems discussed in Sec. V.

In each iteration step, $\phi_w^{(n)}(\tilde{z})$ is substituted into the matched asymptotic profiles in Eq. (49). To obtain $\bar{s}(\bar{y}, \tilde{z}, [\phi_w])$ in the expression for ϕ, integration with respect to $\bar{y}$ is performed numerically using the fourth-order Runge–Kutta method, while all other integrals required for the profiles are obtained by trapezoidal integration. In both numerical integration schemes, an adaptive step size for y is used since the mBLA method invokes two different length scales $\bar{y}$ and $\tilde{y}$ in the CP layer and bulk region, respectively. We have implemented the mBLA solution for the concentration and flow fields in a multiprocessing Python package.[30]

Figure 17 illustrates the convergence of the wall concentration profile with increasing iteration number n for a hard-sphere reference dispersion, as described in Sec. V. The inset shows the measure $\chi(n)$ of the mean relative difference between FEM and mBLA results at the nth iteration step, i.e.,

$$\chi(n) = \sqrt{\frac{1}{N}\sum_i^N \left(\frac{\phi_w^{(n)}(z_i)}{\phi_w^{FEM}(z_i)} - 1 \right)^2}, \tag{D5}$$

where N is the number of equidistant axial positions $\{z_i\}$ with $z_0 = 0$ and $z_{N-1} = L$. The iterations commonly convergence with $\chi(n) \approx 0.03$ for $n > 40$ (see the inset). In all our results, we used $n = 100$ iterations.

DATA AVALIABILITY

The data that support the findings of this study are available from the corresponding author upon reasonable request. Our Python code for calculating ultrafiltration properties using the mBLA method is freely available at doi:10.5281/zenodo.3895786.[30]

REFERENCES

[1]E. A. Mason and H. K. Lonsdale, "Statistical-mechanical theory of membrane transport," J. Membr. Sci. **51**, 1–81 (1990).
[2]M. Mulder, *Basic Principles of Membrane Technology* (Springer Netherlands, 1991).
[3]G. Truskey, F. Yuan, and D. Katz, *Transport Phenomena in Biological Systems* (Pearson Prentice Hall Bioengineering, 2009).
[4]R. H. Davis and D. T. Leighton, "Shear-induced transport of a particle layer along a porous wall," Chem. Eng. Sci. **42**, 275–281 (1987).
[5]M. Mondor and C. Moresoli, "Experimental verification of the shear-induced hydrodynamic diffusion model of crossflow microfiltration, with consideration of the transmembrane pressure axial variation," J. Membr. Sci. **175**, 119–137 (2000).
[6]M. Mondor and C. Moresoli, "Theoretical analysis of the influence of the axial variation of the transmembrane pressure in cross-flow filtration of rigid spheres," J. Membr. Sci. **152**, 71–87 (1999).
[7]V. Nassehi, "Modelling of combined Navier–Stokes and Darcy flows in crossflow membrane filtration," Chem. Eng. Sci. **53**, 1253–1265 (1998).
[8]A. S. Berman, "Laminar flow in channels with porous walls," J. Appl. Phys. **24**, 1232–1235 (1953).
[9]S. W. Yuan and A. B. Finkelstein, "Laminar pipe flow with injection and suction through a porous wall," Trans. Am. Soc. Mech. Eng. **78**, 719–724 (1956).
[10]N. Tilton, D. Martinand, E. Serre, and R. M. Lueptow, "Incorporating Darcy's law for pure solvent flow through porous tubes: Asymptotic solution and numerical simulations," AIChE J. **58**, 2030–2044 (2012).
[11]S. Karode, "Laminar flow in channels with porous walls, revisited," J. Membr. Sci. **191**, 237–241 (2001).
[12]C. Pozrikidis, "Stokes flow through a permeable tube," Arch. Appl. Mech. **80**, 323–333 (2010).
[13]S. J. Mamouri, V. V. Tarabara, and A. Bénard, "Analytical solutions for laminar flow in membrane channels with cylindrical symmetry: Single- and dual-membrane systems," J. Membr. Sci. **523**, 373–384 (2017).
[14]W. F. Blatt, A. Dravid, A. S. Michaels, and L. Nelsen, "Solute polarization and cake formation in membrane ultrafiltration: Causes, consequences, and control techniques," in *Membrane Science and Technology*, edited by J. E. Flinn (Springer US, Boston, MA, 1970), pp. 47–97.
[15]D. R. Trettin and M. R. Doshi, "Limiting flux in ultrafiltration of macromolecular solutions," Chem. Eng. Commun. **4**, 507–522 (1980).
[16]C. A. Romero and R. H. Davis, "Global model of crossflow microfiltration based on hydrodynamic particle diffusion," J. Membr. Sci. **39**, 157–185 (1988).
[17]L. Song and M. Elimelech, "Theory of concentration polarization in crossflow filtration," Faraday Trans. **91**, 3389 (1995).
[18]M. Elimelech and S. Bhattacharjee, "A novel approach for modeling concentration polarization in crossflow membrane filtration based on the equivalence of osmotic pressure model and filtration theory," J. Membr. Sci. **145**, 223–241 (1998).
[19]G. A. Denisov, "Theory of concentration polarization in cross-flow ultrafiltration: Gel-layer model and osmotic-pressure model," J. Membr. Sci. **91**, 173–187 (1994).
[20]R. F. Probstein, J. S. Shen, and W. F. Leung, "Ultrafiltration of macromolecular solutions at high polarization in laminar channel flow," Desalination **24**, 1–16 (1978).
[21]J. J. S. Shen and R. F. Probstein, "On the prediction of limiting flux in laminar ultrafiltration of macromolecular solutions," Ind. Eng. Chem. Fundam. **16**, 459–465 (1977).
[22]R. H. Davis and J. D. Sherwood, "A similarity solution for steady-state crossflow microfiltration," Chem. Eng. Sci. **45**, 3203–3209 (1990).

[23]R. Roa, E. K. Zholkovskiy, and G. Nägele, "Ultrafiltration modeling of non-ionic microgels," Soft Matter **11**, 4106–4122 (2015).
[24]R. Roa, D. Menne, J. Riest, P. Buzatu, E. K. Zholkovskiy, J. K. G. Dhont, M. Wessling, and G. Nägele, "Ultrafiltration of charge-stabilized dispersions at low salinity," Soft Matter **12**, 4638–4653 (2016).
[25]J. Riest, T. Eckert, W. Richtering, and G. Nägele, "Dynamics of suspensions of hydrodynamically structured particles: Analytic theory and applications to experiments," Soft Matter **11**, 2821–2843 (2015).
[26]J. K. G. Dhont, *An Introduction to Dynamics of Colloids* (Elsevier, 1996), p. 660.
[27]R. B. Bird, W. E. Stewart, and E. N. Lightfoot, *Transport Phenomena* (John Wiley & Sons, Inc., 2002).
[28]A. Subramani, S. Kim, and E. Hoek, "Pressure, flow, and concentration profiles in open and spacer-filled membrane channels," J. Membr. Sci. **277**, 7–17 (2006).
[29]B. Marcos, C. Moresoli, J. Skorepova, and B. Vaughan, "CFD modeling of a transient hollow fiber ultrafiltration system for protein concentration," J. Membr. Sci. **337**, 136–144 (2009).
[30]G. W. Park and G. Nägele (2020). "Python code for modified boundary layer solution of concentration-polarization and flow properties in ultrafiltration," Zenodo. https://doi.org/10.5281/zenodo.3895786
[31]A. Pamvouxoglou, P. Bogri, G. Nägele, K. Ohno, and G. Petekidis, "Structure and dynamics in suspensions of soft core-shell colloids in the fluid regime," J. Chem. Phys. **151**, 024901 (2019).
[32]G. C. Abade, B. Cichocki, M. L. Ekiel-Jeżewska, G. Nägele, and E. Wajnryb, "Short-time dynamics of permeable particles in concentrated suspensions," J. Chem. Phys. **132**, 014503 (2010).
[33]V. L. Vilker, C. K. Colton, and K. A. Smith, "The osmotic pressure of concentrated protein solutions: Effect of concentration and ph in saline solutions of bovine serum albumin," J. Colloid Interface Sci. **79**, 548–566 (1981).
[34]E. J. Hinch, *Perturbation Methods* (Cambridge University Press, 1991).
[35]R. F. Probstein, *Physicochemical Hydrodynamics* (John Wiley and Sons, Inc., 1994).
[36]P. Bacchin, D. Si-Hassen, V. Starov, M. J. Clifton, and P. Aimar, "A unifying model for concentration polarization, gel-layer formation and particle deposition in cross-flow membrane filtration of colloidal suspensions," Chem. Eng. Sci. **57**, 77–91 (2002).
[37]P. Bacchin, P. Aimar, and R. Field, "Critical and sustainable fluxes: Theory, experiments and applications," J. Membr. Sci. **281**, 42–69 (2006).
[38]O. C. Zienkiewicz, R. L. Taylor, and P. Nithiarasu, *The Finite Element Method for Fluid Dynamics* (Butterworth Heinemann, 2014), p. 544.
[39]L. Huang and M. T. Morrissey, "Finite element analysis as a tool for crossflow membrane filter simulation," J. Membr. Sci. **155**, 19–30 (1999).
[40]M. Van Dyke, *Perturbation Methods in Fluid Mechanics* (The Parabolic Press, 1975).
[41]V. Berinde, *Iterative Approximation of Fixed Points* (Springer Berlin Heidelberg, 2007).